

High-volume fraction simulations of two-dimensional vesicle suspensions

Bryan Quaife^a, George Biros^a

^a*Institute of Computational Engineering and Sciences,
The University of Texas at Austin, Austin, TX, 78712.*

Abstract

We consider numerical algorithms for the simulation of the rheology of two-dimensional vesicles suspended in a viscous Stokesian fluid. The vesicle evolution dynamics is governed by hydrodynamic and elastic forces. The elastic forces are due to local inextensibility of the vesicle membrane and resistance to bending. Numerically resolving vesicle flows poses several challenges. For example, we need to resolve moving interfaces, address stiffness due to bending, enforce the inextensibility constraint, and efficiently compute the (non-negligible) long-range hydrodynamic interactions.

Our method is based on the work of *Rahimian, Veerapaneni, and Biros*, “*Dynamic simulation of locally inextensible vesicles suspended in an arbitrary two-dimensional domain, a boundary integral method*”, *Journal of Computational Physics*, 229 (18), 2010. It is a boundary integral formulation of the Stokes equations coupled to the interface mass continuity and force balance. We extend the algorithms presented in that paper to increase the robustness of the method and enable simulations with concentrated suspensions.

In particular, we propose a scheme in which both intra-vesicle and inter-vesicle interactions are treated semi-implicitly. In addition we use special integration for near-singular integrals and we introduce a spectrally accurate collision detection scheme. We test the proposed methodologies on both unconfined and confined flows for vesicles whose internal fluid may have a viscosity contrast with the bulk medium. Our experiments demonstrate the importance of treating both intra-vesicle and inter-vesicle interactions accurately.

Keywords: Stokes flow, Suspensions, Particulate flows, Vesicle simulations, Boundary integral method, Fluid membranes, Semi-implicit algorithms, Fluid-structure interaction, Spectral collision detection, Fast multipole methods

1. Introduction

Vesicles are deformable capsules filled with a viscous fluid. The hydrodynamics of vesicles that are suspended in a viscous fluid (henceforth, “*vesicle flows*”) play an important role in many biological phenomena [17, 38]. For example, they are used experimentally to understand properties of biomembranes [36] and red blood cells [8, 13, 24–26]. Here we discuss numerical algorithms for simulating the motion of vesicles in Stokesian fluids in two dimensions. Many features of algorithms designed for particulate flows of vesicle suspensions find applications to other deformable particulate flows, for example deformable capsules, bubbles, drops, and elastic filaments. Vesicle flows are characterized by large deformations, the local inextensibility of a vesicle’s membrane, the conservation of enclosed area due to the incompressibility of the fluid inside the vesicle, and the stiffness related to tension and bending forces. Efficient and accurate numerical methods need to address these issues. It is known that rheology can be sensitive to elastic instabilities that need to be resolved quite accurately in long-horizon simulations [14].

Email addresses: quaife@ices.utexas.edu (Bryan Quaife), gbiros@acm.org (George Biros)

In [29], Pozrikidis presents integral equation formulations for different types of particulate and interfacial viscous flows. In line with our work, integral equation methods have been applied to vesicle suspensions and other similar capsules in two- and three-dimensions by many groups [6, 7, 33, 40, 41, 45, 47–50], to name a few. We focus on algorithms for vesicle flows from our group’s previous work [40], where numerical algorithms for a boundary integral formulation of the vesicle hydrodynamics are presented. In this formulation, a Stokes single-layer potential is coupled with the vesicle membrane forces and results in an integro-differential equation that is constrained by the local inextensibility constraint (see Section 2 for details). In [33], these methods were extended to confined flows and problems with vesicles whose enclosed fluid has a viscosity contrast with the bulk fluid. In [41], we developed algorithms for three-dimensional vesicle flows. To summarize, the main components of the formulation we have used in our prior work are the following: (1) We proposed a time-stepping method in which the inter-vesicle interactions are treated explicitly and the self-vesicle interactions are treated semi-implicitly to remove the bending and tension stiffness; (2) We proposed a spectrally accurate discretization in space for differentiation and integration of smooth functions and weakly singular integrals; (3) We proposed effective preconditioners for the self-vesicle interactions; and (4) We used the fast multipole method to accelerate the integral operators that capture the long range hydrodynamic interactions.

Contributions. In this paper, we continue our efforts towards efficient algorithms for the simulation of vesicle hydrodynamics using boundary integral formulations. We focus on specific issues that are common when simulating high concentration vesicle flows. In particular, we look into stiffness due to *inter-vesicle* dynamics, spectrally accurate collision detection, near-singular integration, and calculating quantities like pressure and stress fields that can be used to define coarse-grained variables. To make things somewhat more precise, let \mathbf{x}_p be the shape parametrization of the p^{th} vesicle (e.g., Lagrangian points or Fourier coefficients), and let \mathbf{u}_p be its velocity. Then the evolution equation for the position of the boundaries of M vesicles can be summarized by

$$\frac{d\mathbf{x}_p}{dt} = \mathbf{u}_\infty(\mathbf{x}_p) + \sum_{q=1}^M \mathbf{u}_p(\mathbf{x}_q), \quad p = 1, \dots, M, \quad (1)$$

where $\mathbf{u}_p(\mathbf{x}_q)$ is the velocity induced on vesicle p due to forces on vesicle q (via hydrodynamic interactions) and $\mathbf{u}_\infty(\mathbf{x}_p)$ is an external velocity field that drives the flow. The term $\mathbf{u}_p(\mathbf{x}_p)$ is the self-interaction term for the vesicle p and $\mathbf{u}_p(\mathbf{x}_q)$, $q \neq p$, are the inter-vesicle interactions.

- **Implicit inter-vesicle interactions.** Most research groups working on vesicle simulations discretize (1) using an explicit time-stepping method. However, (1) is quite stiff due to tension and bending. For this reason, in [40] we introduced time-marching schemes that treat the self-interactions semi-implicitly. For example, a first-order accurate in time scheme (with $\mathbf{u}_\infty = 0$) reads

$$\frac{\mathbf{x}_p^{t+dt} - \mathbf{x}_p^t}{dt} = \tilde{\mathbf{u}}_p(\mathbf{x}_p^{t+dt}) + \sum_{\substack{q=1 \\ q \neq p}}^M \mathbf{u}_p(\mathbf{x}_q^t), \quad p = 1, \dots, M.$$

The velocity $\tilde{\mathbf{u}}_p(\mathbf{x}_p^{t+dt})$ indicates a linearized semi-implicit approximation of the vesicle self-interaction term $\mathbf{u}_p(\mathbf{x}_p)$. Thus, computing \mathbf{x}_p^{t+dt} costs one linear solve per vesicle. This is sufficient to reduced bending and tension stiffness but can be problematic for concentrated suspensions since $\mathbf{u}_p(\mathbf{x}_q)$ also introduces stiffness when vesicles p and q are near each other. In this paper, we introduce a semi-implicit scheme of the form

$$\frac{\mathbf{x}_p^{t+dt} - \mathbf{x}_p^t}{dt} = \sum_{q=1}^M \tilde{\mathbf{u}}_p(\mathbf{x}_q^{t+dt}), \quad p = 1, \dots, M,$$

that treats all coupling terms in a linear semi-implicit way. Thus, one needs to solve a coupled system for all vesicles at every time iteration. We examine the stability of this scheme for first- and second-order time-stepping and we compare it with alternative time-marching methods.

- **Near-singular integration.** When the vesicles come closer together, the hydrodynamic interaction terms (e.g., $\mathbf{u}_p(\mathbf{x}_q)$) require the evaluation of near-singular integrals. This can be quite expensive computationally. Here we use the two-dimensional analogue of the scheme introduced in [43] which allows a fifth-order accurate evaluation of near interactions using optimal work.
- **Spectral collision detection.** Another issue related to concentrated suspensions is collision detection. While it is physically impossible for vesicles to collide with one another or with solid walls in finite time, it is important to detect collisions caused by numerical errors. There exist many efficient algorithms for computing intersections for polygonal domains [11]. Since our spatial discretization is done in high-order accuracy and the vesicle boundaries are C^∞ curves that are spectrally resolved, we propose a collision detection scheme that is based on potential theory and it is ideally suited for smooth geometries. The detection can be done in linear time in the number of degrees of freedom used to represent the vesicle boundaries and requires one evaluation of the free-space Laplace potential. The method is described in Section 3.5.

We test these methodologies in a variety of flows and we study the stability and accuracy of the overall algorithm. As a secondary contribution, we also provide a scheme for computing average pressures and stresses in regions of interest, described in Section 4. The results of our tests are described in Section 5 in which we test problems with viscosity contrast, confined flows, and concentrated suspension flows.

Limitations. The main limitation is that the method is developed in two dimensions. Although several flows can be described to good accuracy under a two-dimensional approximation, a lot of interesting phenomena occur only in three-dimensional, especially for concentrated suspensions. The extensions that we present in this paper do not rely on two-dimensions, and using these methods in three-dimensions is a problem of implementation. In particular, the spectral collision detection scheme only relies on a standard potential theory result that holds in three-dimensions, and the fast multiple method. The time integrators also naturally extend to three-dimensions, but more work is required to precondition the linear operators that appear upon time discretization. The near-singular integration details have been discussed for generic surfaces in [43], but several optimizations are possible for shapes represented by spherical harmonics, which we use in our three-dimensional schemes.

Another major limitation is that we do not use time and space adaptivity. Those two are essential for efficient robust solvers that can be used by non-experts. Currently, we select the time step size by a trial and error process. We are currently working on devising time and space adaptive methods.

Finally, the method is most suitable for Stokesian bulk fluids. If inertial or viscoelastic effects are important, a boundary integral formulation cannot be used.

Related work. There is extensive work on vesicle simulations. Our list here is by no means exhaustive, but it includes some of the work that is most relative to ours. Pozrikidis offers an excellent review of numerical methods for interfacial dynamics in a Stokes flow [29]. Capsules similar to ours have been simulated in concentrated suspensions in [6, 7, 22, 46, 49, 50]. Also, in [20, 21, 31], high concentration suspensions of a different kind of capsule are considered, but these capsules do not resist bending; therefore, the governing equations are far less stiff. While some of these methods use spectral methods, most of them use an explicit time stepping method which results in a strict restriction on the time step size. In order to allow for larger time steps, a Jacobian-free Newton method outlined in [4] was applied to an implicit discretization of droplets submerged in a Stokes flow [3]. While this allows for larger time steps, it requires the solution of nonlinear equations which can be computationally expensive, and this technique has not been tested on vesicle suspensions. Work that uses a combination of implicit and explicit methods to study the dynamics of a single vesicle include [44, 47], but both these methods require multiple solves per time step since they use a predictor-corrector scheme. In this paper, we remove the stiffness with a semi-implicit method which only requires solving one linear equation per time step. These methods have been applied to a single vesicle in [37, 44] and are extended to multiple vesicles, where the only the self-interactions are treated semi-implicitly in [33, 40, 48]. However, with multiple vesicles, we are unaware of any work that couples all the vesicles and solid walls implicitly and achieves more than first-order accuracy in time.

Evaluating layer potentials close to their sources is an active area of research. Popular methods to evaluate near-singular integrals include upsampling or high-order quadrature rules [9, 19], and singularity subtraction or partitions of unity [6, 28, 49]. Some of these methods claim to achieve up to third-order accuracy, but they do not report timings or accuracies. Therefore, the cost required to achieve the accuracies we desire is unclear. Moreover, these methods often depend on the dimension of the problem and nature of the singularity. A more recent technique is QBX [16] which can deliver arbitrary accuracy, but is difficult to implement and we anticipate it will be too expensive for problems with moving boundaries. The method we use naturally extends to three dimensions and we have successfully used it for a variety of near-singular integrals.

Outline of the paper. In Section 2, we summarize the formulation of our problem. In Section 3, we discuss the spatio-temporal discretization including the new scheme that semi-implicitly couples the vesicle updates, the near-singular evaluation (Section 3.4), and the collision detection (Section 3.5). The average pressure and stress calculations are in Section 4 and the results are described in Section 5.

2. Formulation

Let us first define the main variables used to model vesicle flows. Neglecting inertial forces, the dynamics of vesicle flows is fully characterized by the position of the interface $\mathbf{x}(s, t) \in \gamma$, where s is the arclength, t is time, and γ is the membrane of the vesicle. The position is determined by solving a moving interface problem that models the mechanical interactions between the viscous incompressible fluid in the exterior and interior of the vesicle (with viscosity μ) and the vesicle membrane. Given $\mathbf{x}(s, t)$, derived variables include the fluid velocity \mathbf{u} , the fluid stress T , the pressure p , and the membrane tension σ . In addition, if \mathbf{n} is the outward normal to the vesicle membrane γ , then the stress jump $\mathbf{f}(\mathbf{x}) = \llbracket T \rrbracket \mathbf{n}$, which is a nonlinear function of the position \mathbf{x} , is equal to the sum of a force due to the vesicle membrane bending modulus κ_b and a force due to the tension σ . For wall-confined flows, additional parameters are the prescribed wall velocity $\mathbf{U}(\mathbf{x}, t)$, $\mathbf{x} \in \Gamma$.

Given these definitions, the equations for a single vesicle flow are given

$$\begin{aligned}
\mu \nabla \cdot (\nabla \mathbf{u} + \nabla \mathbf{u}^T) - \nabla p(\mathbf{x}) &= 0, & \mathbf{x} \in \Omega \setminus \gamma, & \text{conservation of momentum,} \\
\nabla \cdot \mathbf{u}(\mathbf{x}) &= 0, & \mathbf{x} \in \Omega \setminus \gamma, & \text{conservation of mass,} \\
\mathbf{x}_s \cdot \mathbf{u}_s &= 0, & \mathbf{x} \in \gamma, & \text{membrane inextensibility,} \\
\mathbf{u}(\mathbf{x}, t) &= \dot{\mathbf{x}}(t), & \mathbf{x} \in \gamma, & \text{velocity continuity,} \\
\mathbf{f}(\mathbf{x}) &= -\kappa_b \mathbf{x}_{ssss} + (\sigma(\mathbf{x}) \mathbf{x}_s)_s, & \mathbf{x} \in \gamma, & \text{nonzero stress jump,} \\
\mathbf{u}(\mathbf{x}, t) &= \mathbf{U}(\mathbf{x}, t), & \mathbf{x} \in \Gamma, & \text{wall velocity.}
\end{aligned} \tag{2}$$

The viscosity contrast is taken to be constant inside each vesicle. However, these values can differ from the viscosity of the exterior fluid. We also consider a different stress jump that corresponds to a prescribed intrinsic curvature for the vesicle membrane. The modification to the formulation and results are reported in Appendix C. In the case of a problem with M vesicles with interfaces denoted by $\{\gamma_p\}_{p=1}^M$, we define

$$\gamma = \bigcup_{p=1}^M \gamma_p.$$

Finally, if Ω is m-ply connected, we let Γ_0 denote the connected component of $\Gamma = \Gamma_0 \cup \Gamma_1 \cup \dots \cup \Gamma_m$ that surrounds all the other connected components of Γ .

There exist many numerical methods for solving interface evolution equations like (2). Since the viscosity is piecewise constant with a discontinuity along the interface, we opt for an integral equation formulation using the Stokes free-space Green's function. Next, following [33], we introduce integral and differential operators that we will need to reformulate (2).

2.1. Integral equation formulation

We give the formulation for the general case in which we have viscosity contrast between the interior and exterior fluid (μ_0 is the viscosity of the exterior fluid, μ_p is the viscosity of the interior fluid for vesicle p , and $\nu_p = \mu_p/\mu_0$), and solid boundaries with a prescribed velocity. First we introduce \mathcal{S}_{pq} and \mathcal{D}_{pq} , the single- and double-layer potentials for Stokes flow, where the constant factors are chosen so that our formulation is in agreement with Pozrikidis [30, equation 2.2]. The subscripts denote the potentials induced by a hydrodynamic density on the membrane of vesicle q and evaluated on the membrane of vesicle p :

$$\begin{aligned}\mathcal{S}_{pq}[\mathbf{f}](\mathbf{x}) &:= \frac{1}{4\pi\mu_0} \int_{\gamma_q} \left(-\mathbf{I} \log \rho + \frac{\mathbf{r} \otimes \mathbf{r}}{\rho^2} \right) \mathbf{f} \, ds_{\mathbf{y}}, & \mathbf{x} \in \gamma_p, \\ \mathcal{D}_{pq}[\mathbf{u}](\mathbf{x}) &:= \frac{1-\nu_q}{\pi} \int_{\gamma_q} \frac{\mathbf{r} \cdot \mathbf{n}}{\rho^2} \frac{\mathbf{r} \otimes \mathbf{r}}{\rho^2} \mathbf{u} \, ds_{\mathbf{y}}, & \mathbf{x} \in \gamma_p,\end{aligned}$$

where $\mathbf{r} = \mathbf{x} - \mathbf{y}$, and $\rho = \|\mathbf{r}\|_2$. Also, we define

$$\mathcal{S}_p := \mathcal{S}_{pp} \quad \text{and} \quad \mathcal{D}_p := \mathcal{D}_{pp},$$

to indicate vesicle self-interactions. Next, we define

$$\begin{aligned}\mathcal{E}_{pq}[\mathbf{f}, \mathbf{u}](\mathbf{x}) &= \mathcal{S}_{pq}[\mathbf{f}](\mathbf{x}) + \mathcal{D}_{pq}[\mathbf{u}](\mathbf{x}), & \mathbf{x} \in \gamma_p, \\ \mathcal{E}_p[\mathbf{f}, \mathbf{u}](\mathbf{x}) &= \sum_{q=1}^M \mathcal{E}_{pq}[\mathbf{f}, \mathbf{u}](\mathbf{x}), & \mathbf{x} \in \gamma_p.\end{aligned}$$

\mathcal{B} is the completed double-layer operator for confined Stokes flow with density $\boldsymbol{\eta}$

$$\mathcal{B}[\boldsymbol{\eta}](\mathbf{x}) = \mathcal{D}_{\Gamma}[\boldsymbol{\eta}](\mathbf{x}) + \sum_{q=1}^M R[\xi_q(\boldsymbol{\eta}), \mathbf{c}_q](\mathbf{x}) + \sum_{q=1}^M S[\boldsymbol{\lambda}_q(\boldsymbol{\eta}), \mathbf{c}_q](\mathbf{x}), \quad \mathbf{x} \in \gamma \cup \Gamma.$$

If $\mathbf{x} \in \Gamma_0$, the rank one modification $\mathcal{N}_0[\boldsymbol{\eta}](\mathbf{x}) = \int_{\Gamma_0} (\mathbf{n}(\mathbf{x}) \otimes \mathbf{n}(\mathbf{y})) \boldsymbol{\eta}(\mathbf{y}) \, ds_{\mathbf{y}}$ is added to \mathcal{B} which removes the one-dimensional null space of the corresponding integral equation [27]. The Stokeslets and rotlets are defined as

$$S[\boldsymbol{\lambda}_q(\boldsymbol{\eta}), \mathbf{c}_q](\mathbf{x}) = \frac{1}{4\pi\mu_0} \left(\log \rho + \frac{\mathbf{r} \otimes \mathbf{r}}{\rho^2} \right) \boldsymbol{\lambda}_q(\boldsymbol{\eta}) \quad \text{and} \quad R[\xi_q(\boldsymbol{\eta}), \mathbf{c}_q](\mathbf{x}) = \frac{\xi_q(\boldsymbol{\eta})}{\mu_0} \frac{\mathbf{r}^\perp}{\rho^2},$$

where \mathbf{c}_q is a point inside ω_q , ω_q is the interior of vesicle q , $\mathbf{r} = \mathbf{x} - \mathbf{c}_q$, and $\mathbf{r}^\perp = (r_2, -r_1)$. The operator \mathcal{B} satisfies the jump condition

$$\lim_{\substack{\mathbf{x} \rightarrow \mathbf{x}_0 \\ \mathbf{x} \in \Omega}} \mathcal{B}[\boldsymbol{\eta}](\mathbf{x}) = -\frac{1}{2} \boldsymbol{\eta}(\mathbf{x}_0) + \mathcal{B}[\boldsymbol{\eta}](\mathbf{x}_0), \quad \mathbf{x}_0 \in \Gamma,$$

and the size of the Stokeslets and rotlets are

$$\boldsymbol{\lambda}_{q,i} = \frac{1}{2\pi} \int_{\gamma_q} \boldsymbol{\eta}_i(\mathbf{y}) \, ds_{\mathbf{y}}, \quad i = 1, 2 \quad \text{and} \quad \xi_q = \frac{1}{2\pi} \int_{\gamma_q} \mathbf{y}^\perp \boldsymbol{\eta}(\mathbf{y}) \, ds_{\mathbf{y}}.$$

The inextensibility constraint is written in operator form as

$$\mathcal{P}[\mathbf{u}](\mathbf{x}) = \mathbf{x}_s \cdot \mathbf{u}_s.$$

Putting everything together, the integral formulation equation of (2) is given by [33]

$$(1 + \nu_p) \mathbf{u}(\mathbf{x}) = \mathcal{E}_p[\mathbf{f}, \mathbf{u}](\mathbf{x}) + \mathcal{B}_p[\boldsymbol{\eta}](\mathbf{x}), \quad \mathbf{x} \in \gamma_p, \quad (3a)$$

$$\mathcal{P}[\mathbf{u}](\mathbf{x}) = 0, \quad \mathbf{x} \in \gamma_p, \quad (3b)$$

$$\mathbf{U}(\mathbf{x}) = -\frac{1}{2} \boldsymbol{\eta}(\mathbf{x}) + \mathcal{E}_{\Gamma}[\mathbf{f}, \mathbf{u}](\mathbf{x}) + \mathcal{B}[\boldsymbol{\eta}](\mathbf{x}), \quad \mathbf{x} \in \Gamma, \quad (3c)$$

where \mathbf{f} is the hydrodynamic density, which in our case is the stress jump on the vesicle interface, which also is referred to as the traction jump, and is given by

$$\mathbf{f} = -\kappa_b \mathbf{x}_{ssss} + (\sigma \mathbf{x}_s)_s.$$

Since $\mathbf{u} = dx/dt$ and \mathbf{f} depends on σ and \mathbf{x} , (3) is a system of integro-differential-algebraic equations for \mathbf{x} , σ , and η .

3. Method

Following [33], we use a Lagrangian formulation in which we track the position of material points on γ using multistep implicit-explicit (IMEX) methods [2] to discretize (3) in time. We use Nyström-type quadrature rules to discretize integral operators and Fourier differentiation to compute derivatives with respect to the membrane parametrization.

3.1. Spatial Discretization

Let $\mathbf{x}(\alpha)$, with $\alpha \in (0, 2\pi]$, be a parametrization of the interface γ_p , $\{\alpha_k = 2k\pi/n\}_{k=1}^n$ be n material points, and

$$\mathbf{x}(\alpha) = \sum_{k=-n/2+1}^{n/2} \hat{\mathbf{x}}(k) e^{ik\alpha}.$$

Using the FFT to compute $\hat{\mathbf{x}}$, we compute derivatives of \mathbf{x} with spectral accuracy, assuming that γ belongs to C^∞ . In particular, we can compute the arclength derivative with spectral accuracy since

$$\frac{\partial}{\partial s} = \frac{\partial \alpha}{\partial s} \frac{\partial}{\partial \alpha} = \frac{1}{\|\partial \mathbf{x} / \partial \alpha\|} \frac{\partial}{\partial \alpha},$$

where s is the arclength parametrization.

Since the single-layer potential \mathcal{S} has a logarithmic singularity, we use the hybrid Gauss-trapezoid quadrature rule given in Table 8 of [1]. The error of this quadrature rule is $\mathcal{O}(h^8 \log h)$ for integrands with logarithmic singularities. Letting $\mathbf{x}_k = \mathbf{x}(\alpha_k)$, the quadrature rule is

$$\mathcal{S}[\mathbf{f}](\mathbf{x}) \approx \sum_{k=1}^{n+m} w_k \mathcal{S}(\mathbf{x}, \mathbf{x}_k) \mathbf{f}(\mathbf{x}_k) \|\mathbf{x}_{\alpha, k}\|,$$

where n is the number of nodes, m is a number of additional quadrature nodes, w_k are the quadrature weights, \mathbf{x}_k are the quadrature abscissae, and \mathbf{x}_α is $\partial \mathbf{x} / \partial \alpha$. The first n abscissae are the usual equispaced quadrature points. Then, the other m , which is determined by the desired order of convergence for the integral, are additional quadrature abscissas clustered around the singularity.

The double-layer potential has no singularity in two dimensions since

$$\lim_{\substack{\mathbf{x}' \rightarrow \mathbf{x} \\ \mathbf{x}' \in \gamma}} D(\mathbf{x}', \mathbf{x}) = \frac{\kappa(\mathbf{x})}{2\pi} (\mathbf{t}(\mathbf{x}) \otimes \mathbf{t}(\mathbf{x})), \quad \mathbf{x} \in \gamma,$$

where κ is the curvature and \mathbf{t} is the unit tangent. Thus, a composite trapezoid rule will give spectral accuracy since the integrand is periodic and smooth.

3.2. Time discretization

Time derivatives are discretized as

$$\frac{d\mathbf{x}}{dt} \approx \frac{\beta\mathbf{x}^{N+1} - \mathbf{x}^0}{\Delta t},$$

where \mathbf{x}^0 is a linear combination of previous time steps. Operators and terms that are treated explicitly are discretized at \mathbf{x}^e which is also a linear combination of previous time steps. The simplest IMEX method is IMEX Euler which is given by $\beta = 1$, $\mathbf{x}^0 = \mathbf{x}^N$, and $\mathbf{x}^e = \mathbf{x}^N$. The second-order time integrator we use is given by $\beta = 3/2$,

$$\mathbf{x}^0 = 2\mathbf{x}^N - \frac{1}{2}\mathbf{x}^{N-1}, \quad \mathbf{x}^e = 2\mathbf{x}^N - \mathbf{x}^{N-1}.$$

To avoid significant time stepping constraints, we treat the bending term \mathbf{f}_b and tension term \mathbf{f}_σ semi-implicitly. An approximation for the position and tension of vesicle p at time $N + 1$ satisfies

$$\frac{\alpha_p}{\Delta t}(\beta\mathbf{x}_p^{N+1} - \mathbf{x}_p^0) = \mathcal{S}_p^e \mathbf{f}_p^{N+1} + \mathcal{D}_p^e \mathbf{u}_p^{N+1} + \mathcal{B}_p[\boldsymbol{\eta}^N] + \sum_{\substack{q=1 \\ q \neq p}}^M \mathcal{E}_{pq}^e[\mathbf{f}_q^N, \mathbf{u}_q^N], \quad \mathbf{x} \in \gamma_p, \quad (4a)$$

$$\beta\mathcal{P}^e \mathbf{x}_p^{N+1} = \mathcal{P}^e \mathbf{x}_p^0, \quad \mathbf{x} \in \gamma_p, \quad (4b)$$

$$U(\mathbf{x}) = -\frac{1}{2}\boldsymbol{\eta}^N(\mathbf{x}) + \mathcal{E}_\Gamma^e[\mathbf{f}^N, \mathbf{u}^N](\mathbf{x}) + \mathcal{B}[\boldsymbol{\eta}^N](\mathbf{x}) + \mathcal{N}_0[\boldsymbol{\eta}^N](\mathbf{x}), \quad \mathbf{x} \in \Gamma, \quad (4c)$$

$$\mathbf{u}_p^{N+1} = \frac{\beta\mathbf{x}_p^{N+1} - \mathbf{x}_p^0}{\Delta t}, \quad \mathbf{x} \in \gamma_p, \quad (4d)$$

where $\alpha_p = (1 + \nu_p)/2$, and operators with a superscript e are discretized at \mathbf{x}^e . Note that (4) has explicit vesicle-vesicle and vesicle-boundary interactions. That is, we are approximating the solution of (3) with the solution of a problem where the vesicles are fully decoupled from one another and from the boundary. To solve (4), we first find $\boldsymbol{\eta}^N$ by solving (4c) and then solve (4a) and (4b) for the new position and tension of each vesicle independently of all the others.

In high-concentration flows, a new source of stiffness arises. As two vesicles approach one another, \mathcal{E}_{pq} becomes increasingly large. A similar result holds for vesicle-boundary interactions where \mathcal{B}_p introduces stiffness. We propose the new method with semi-implicit vesicle-vesicle and vesicle-boundary interactions (the differences with (4) being highlighted in red)

$$\frac{\alpha_p}{\Delta t}(\beta\mathbf{x}_p^{N+1} - \mathbf{x}_p^0) = \mathcal{S}_p^e \mathbf{f}_p^{N+1} + \mathcal{D}_p^e \mathbf{u}_p^{N+1} + \mathcal{B}_p[\boldsymbol{\eta}^{N+1}] + \sum_{\substack{q=1 \\ q \neq p}}^M \mathcal{E}_{pq}^e[\mathbf{f}_q^{N+1}, \mathbf{u}_q^{N+1}], \quad \mathbf{x} \in \gamma_p, \quad (5a)$$

$$\beta\mathcal{P}^e \mathbf{x}_p^{N+1} = \mathcal{P}^e \mathbf{x}_p^0, \quad \mathbf{x} \in \gamma_p, \quad (5b)$$

$$U(\mathbf{x}) = -\frac{1}{2}\boldsymbol{\eta}^{N+1}(\mathbf{x}) + \mathcal{E}_\Gamma^e[\mathbf{f}^{N+1}, \mathbf{u}^{N+1}](\mathbf{x}) + \mathcal{B}[\boldsymbol{\eta}^{N+1}](\mathbf{x}) + \mathcal{N}_0[\boldsymbol{\eta}^{N+1}](\mathbf{x}), \quad \mathbf{x} \in \Gamma, \quad (5c)$$

$$\mathbf{u}_p^{N+1} = \frac{\beta\mathbf{x}_p^{N+1} - \mathbf{x}_p^0}{\Delta t}, \quad \mathbf{x} \in \gamma_p. \quad (5d)$$

Unlike in (4), vesicles in (5) are implicitly coupled since the operator \mathcal{E}_{pq}^e is applied to \mathbf{f}_q^{N+1} and \mathbf{u}_q^{N+1} . Similarly, the operator \mathcal{B}_p implicitly couples the vesicles to the solid walls. Equation (5) is still an approximation of (3), but its benefit is that it is experimentally a more stable method (see Sections 5.2 and 5.5).

Since (5) is fully coupled, it is too expensive to solve without preconditioning. Roughly speaking, the number of GMRES iterations depends on the sizes of \mathcal{E}_{pp} and \mathcal{E}_{pq} and the latter depends on the inter-vesicle proximity. We apply preconditioned GMRES [35] to (5) where we use the block-diagonal preconditioner.

The number of GMRES iterations depends on the minimum inter-vesicle distance, but this preconditioned linear system experimentally results in mesh-independence¹.

To test the preconditioner, one step of a Taylor-Green flow is done with the number of points per vesicle ranging from 16 to 128 (Table 1). We solve (5) to a tolerance of 10^{-8} with and without preconditioning. The required GMRES iterations for the block-diagonal solver grows almost linearly and the results are consistent with those reported in [33]. The implicit solver without preconditioning requires an unacceptable number of GMRES iterations, but with preconditioning, we see that the required number of GMRES steps is independent of N ². Using the block-diagonal preconditioner will not result in a speedup unless we precompute and store the block diagonal preconditioner. We perform this precomputation for all the experiments in Section 5.

N	Block-Diagonal	Unpreconditioned Implicit	Preconditioned Implicit
16	46	315	18
32	79	341	15
64	164	882	15
128	294	2117	15

Table 1: The number of GMRES iterations required to take one time step of a Taylor-Green flow using semi-implicit inter-vesicle interactions (5). N is the number of discretization points per vesicle, the second column is the number of GMRES iterations to invert the block-diagonal preconditioner, the third column is the number of unpreconditioned GMRES iterations, and the final column is the number of preconditioned GMRES iterations. Notice that without preconditioning, the number of iterations quickly grows while the preconditioned linear system is mesh-independent.

We have also observed experimentally that when vesicles are close, treating inter-vesicle interactions explicitly with second-order time stepping is unconditionally unstable. We have experimented with time step sizes of varying orders of magnitude and each experiment inevitably becomes unstable. However, scheme (5) with second-order time stepping is stable once Δt is small enough for the simulation under consideration.

3.3. Fast summation

For high-concentration flows, the most expensive part of the simulation is evaluating the integral operators \mathcal{S} and \mathcal{D} . The single-layer potential \mathcal{S} can be written as

$$\begin{aligned} \frac{1}{4\pi\mu_0} \int_{\gamma} \left(-\mathbf{I} \log \rho + \frac{\mathbf{r} \otimes \mathbf{r}}{\rho^2} \right) \mathbf{f} ds &= -\frac{1}{4\pi\mu_0} \int_{\gamma} (\log \rho) \mathbf{f} ds + \frac{1}{4\pi\mu_0} \int_{\gamma} \left(\frac{\mathbf{r} \cdot \mathbf{f}}{\rho^2} \right) \mathbf{r} ds \\ &= -\frac{1}{4\pi\mu_0} \int_{\gamma} (\log \rho) \mathbf{f} ds + \frac{1}{4\pi\mu_0} \int_{\gamma} \frac{\mathbf{r}}{\rho^2} (\mathbf{x} \cdot \mathbf{f}) ds_{\mathbf{y}} - \frac{1}{4\pi\mu_0} \int_{\gamma} \frac{\mathbf{r}}{\rho^2} (\mathbf{y} \cdot \mathbf{f}) ds_{\mathbf{y}}, \end{aligned}$$

which can be computed with three Laplace FMM applications. We also use the FMM to evaluate the single-layer potential at arbitrary target locations by assigning a charge of zero to these locations. Unfortunately, the double-layer potential can not be decomposed into a sequence of Laplace single- and double-layer potentials. Future work involves using the kernel-independent FMM [42] to accelerate evaluating the double-layer potential.

¹We experimented with multigrid preconditioners [32] but mesh-independence was only achieved for computationally expensive preconditioners.

²Notice, however, that the number of GMRES iterations will depend on how close the vesicles are to one another as this determines the overall spectrum structure of the operator. But for a given flow, the method is independent of N .

3.4. Near-singular integration

Another difficulty with high-concentration simulations is the evaluation of layer potentials at points close to a boundary. Integral operators \mathcal{D} and \mathcal{S} can be approximated with high accuracy using the trapezoid rule if the target point is sufficiently far from the source points. As the target point approaches the vesicle, more points are required to achieve the same accuracy, and, the required number of points for a fixed error grows without bound (Appendix A). A near-singular integration strategy that guarantees a uniform accuracy for all target points is required.

We adopt the strategy from [43] since it is not depend on the nature of the integrand and it is simple to implement. Suppose that a vesicle γ is discretized with N points and that the resulting arclength term is of size h . Let $d(\mathbf{x}, \gamma) = \inf_{\mathbf{y} \in \gamma} \|\mathbf{x} - \mathbf{y}\|$ be the distance from \mathbf{x} to γ . We define the far zone of γ as $\Omega_1 = \{\mathbf{x} \mid d(\mathbf{x}, \gamma) \geq h\}$, and the near zone of γ as $\Omega_0 = \{\mathbf{x} \mid d(\mathbf{x}, \gamma) < h\}$. The near and far zones can be constructed efficiently using a quadtree-structure, similar to the near-field and far-field interactions in fast multipole codes.

For $\mathbf{x} \in \Omega_1$, the trapezoid rule with $N^{3/2}$ points guarantees that the error for \mathcal{S} is $\mathcal{O}(h^{M/2-2})$ and for \mathcal{D} is $\mathcal{O}(h^{M/2-4})$, where the density function (in our case, either \mathbf{f} or $\boldsymbol{\eta}$) belongs to C^M . These error bounds are proved in Appendix A. For a target point \mathbf{x} in the near zone, we first find the closest boundary point, \mathbf{x}_0 , using two applications of Newton's method with the initial guess being the closest discretization point to \mathbf{x} . We then place m interpolation points at the points $\mathbf{x}_j = \mathbf{x}_0 + j\beta h(\mathbf{x} - \mathbf{x}_0)/\|\mathbf{x} - \mathbf{x}_0\|$ for $j = 0, \dots, m$, where β is slightly larger than 1 to guarantee that all the interpolation points are in the far zone (left plot of Figure 1). The layer potential is evaluated at \mathbf{x}_0 using a local interpolant with N_{int} points on γ and evaluated at \mathbf{x}_j , $j = 1, \dots, m$ using the $N^{3/2}$ -point trapezoid rule. Then, a one-dimensional Lagrange interpolation assigns a value to the layer potential at \mathbf{x} . Note that the proposed scheme can become more accurate by using interpolation schemes that compute derivatives of the solution and building more accurate polynomial interpolations. This, however, would significantly complicate the implementation. Pseudocode for this algorithm is given in Algorithm 1. In Appendix A, we show that the error of our algorithm applied to the single-layer potential \mathcal{S} is

$$\mathcal{O}\left(h^{\min(N_{\text{int}}-1, m, \frac{M}{2}-2)}\right),$$

and applied to the double-layer potential \mathcal{D} is

$$\mathcal{O}\left(h^{\min(N_{\text{int}}-1, m, \frac{M}{2}-4)}\right).$$

Algorithm 1 *LayerPotential*($\gamma, \mathbf{f}, \mathbf{u}, \Omega_0, \Omega_1$)

for all $\mathbf{x} \in \Omega_1$ do	Loop over far zone
$\mathbf{u} = \text{trapezoid}(\gamma, \mathbf{x}, \mathbf{f})$	Apply the $N^{3/2}$ -point trapezoid rule
end for	
for all $\mathbf{x} \in \Omega_0$ do	Loop over near zone
$\mathbf{x}_0 = \text{argmin } d(\mathbf{x}, \gamma)$	Find the point on γ closest to \mathbf{x}
$\mathbf{u}_0 = \text{interpolate}(\mathbf{x}_0, \mathbf{u}_1, \dots, \mathbf{u}_{N_{\text{int}}})$	Interpolate \mathbf{u} at \mathbf{x}_0
for $j = 1, \dots, m$ do	
$\mathbf{x}_j = \mathbf{x}_0 + j\beta h(\mathbf{x} - \mathbf{x}_0)/\ \mathbf{x} - \mathbf{x}_0\ $	Define Lagrange interpolation points
$\mathbf{u}_j = \text{trapezoid}(\gamma, \mathbf{x}_j, \mathbf{f})$	Evaluate layer potential at \mathbf{x}_j
end for	
$\mathbf{u} = \text{interpolate}(\mathbf{x}, \mathbf{u}_0, \dots, \mathbf{u}_m)$	Compute \mathbf{u} using Lagrange interpolation
end for	
return \mathbf{u}	Return the layer potential at all target points

We test our near-singular integration with three examples. In all the examples, 32 target points are placed in Ω_0 for $N = 16, \dots, 512$. The boundary is a 3 : 2 ellipse, the boundary values are interpolated

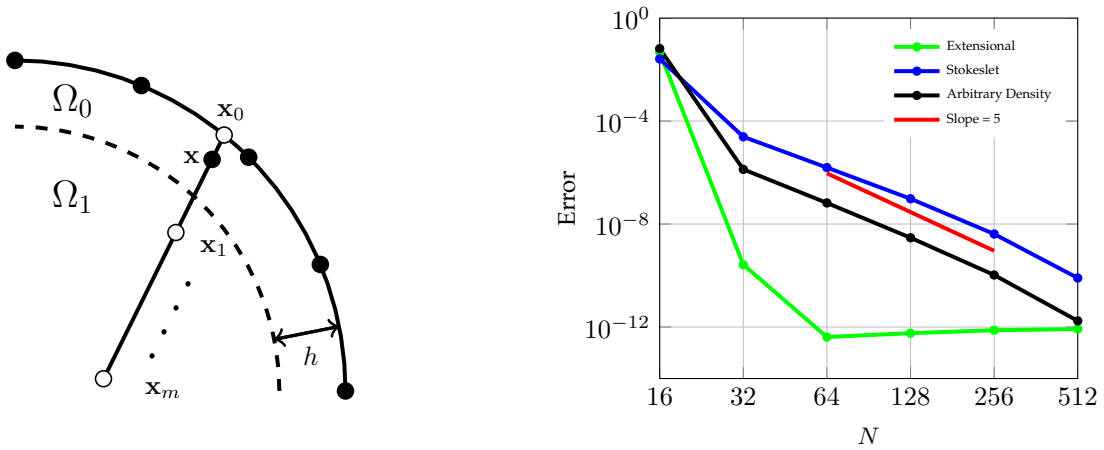


Figure 1: Left: Lagrange interpolation points in Ω_1 and γ are used to approximate layer potentials at $\mathbf{x} \in \Omega_0$. The value at \mathbf{x}_0 uses an interpolant from neighboring points on the boundary. All other interpolation points are in Ω_1 so that the $N^{3/2}$ -point trapezoid rule is sufficiently accurate. Right: Here we report convergence rates. For the blue and the black curves, the expected order of convergence is 5. We obtain 4.7 and 5.0, respectively. As the green curve corresponds to a linear flow, Lagrange interpolation gives exact values. Hence, machine accuracy is reached once N is sufficiently large.

with $N_{\text{int}} = 6$ points, and the Lagrange interpolation uses $m = 6$ points. Since $m = N_{\text{int}}$, we are using one more point to interpolate in the direction coming off of γ . We do this because the interpolant that is coming off of the vesicle is always evaluated near the first interpolation point. Thus, it may suffer from the Runge phenomenon (we have observed this experimentally). This is not the case for the local interpolation used to find $\mathbf{u}(\mathbf{x}_0)$ since \mathbf{x}_0 is located near the middle of the local interpolation points. For the first two examples, we compute the density function of \mathcal{S} for the two solutions of the Stokes equations:

$$\mathbf{u}(\mathbf{x}) = (x, -y),$$

$$\mathbf{u}(\mathbf{x}) = \left(-\log |\mathbf{x}| + \frac{\mathbf{x} \otimes \mathbf{x}}{|\mathbf{x}|^2} \right) \begin{bmatrix} 1 \\ 1 \end{bmatrix}.$$

For the third example, we pick an arbitrary density function and compare the results from near-singular integration with the results from an over-refined trapezoid rule. The error for all three examples is reported in Figure 1. For the extensional flow $\mathbf{u} = (x, -y)$, the Lagrange interpolation is exact since the flow is linear and the error decays faster than the other examples. For the other examples, the error is close to fifth-order which agrees with the order of accuracy of the near-singular integration

If we have M vesicles and N points per vesicle, the major costs of the near-singular integration algorithm are:

- *Upsampling each vesicle from N to $N^{3/2}$ points:* Using the FFT, this requires $\mathcal{O}(MN^{3/2} \log N)$ operations.
- *Applying the $N^{3/2}$ -point quadrature rule to Ω_1 :* With the FMM, this requires $\mathcal{O}(MN^{3/2} + MN)$ operations, and without the FMM, this requires $\mathcal{O}(M^2 N^{5/2})$ operations.
- *Evaluating the layer potential in Ω_0 :* Assuming there are $\mathcal{O}(1)$ points in the near zone, this requires $\mathcal{O}(MN^{3/2})$ operations.

The algorithm can be further sped up by introducing the intermediate and far zones [43]. The intermediate zone is $\Omega_1 = \{\mathbf{x} \mid d(\mathbf{x}, \gamma) \in (\sqrt{h}, h)\}$ and the far zone is $\Omega_2 = \{\mathbf{x} \mid d(\mathbf{x}, \gamma) \geq \sqrt{h}\}$. Then, the same accuracy can be achieved by using the $N^{3/2}$ -point trapezoid rule in Ω_1 and the N -point trapezoid rule in Ω_2 . While this would reduce the constant of the complexity, it does not change the overall order and complicates the implementation.

3.5. Collision detection

Even with semi-implicit treatment of inter-vesicle interactions, due to time discretization errors, the vesicles can come so close that they collide or cross a solid wall.³ There has been a lot of work in collision detection [11, 34], but they are not spectrally accurate or require complex surface-surface intersections. Most methods construct piecewise approximations to the boundaries to simplify the detection of collisions. Since our vesicles and solid walls are periodic, we can use some nice properties of layer potentials to create a spectrally accurate collision detector. We use the classic potential theory result [15]

$$I_\Gamma(\mathbf{x}) = \frac{1}{2\pi} \int_\Gamma \frac{\partial}{\partial \mathbf{n}_y} \log |\mathbf{x} - \mathbf{y}| ds_y = \begin{cases} 1 & \mathbf{x} \in \Omega, \\ \frac{1}{2} & \mathbf{x} \in \Gamma, \\ 0 & \mathbf{x} \in \mathbf{R}^2 \setminus \bar{\Omega}, \end{cases} \quad (6)$$

where $\Omega \subset \mathbf{R}^2$ is bounded with a smooth boundary Γ , and \mathbf{n}_y is the outward pointing normal. We apply (6) to the configuration of the vesicles and the solid walls by computing $I_X(\mathbf{x}) = I_{\gamma_1}(\mathbf{x}) + \dots + I_{\gamma_M} + I_\Gamma$ for all $\mathbf{x} \in \gamma$. The maximum value of $I_X(\mathbf{x})$ is $3/2$ for confined flows and $1/2$ for unconfined flows if vesicles have not crossed and have not left the domain. The maximum value of $I_X(\mathbf{x})$ will be at least $3/2$ for unconfined flows, and at least $5/2$ for confined flows if vesicles have crossed or left the domain. We note that $I_X(\mathbf{x})$ can be evaluated accurately using our near-singular integration scheme, and in linear time using the FMM.

We can use $I_X(\mathbf{x})$ to create a simple adaptive time-stepping method. At each time step, we check for collisions. If a collision has occurred, we initialize the simulation at a previous time step with a time step half the size. We are currently implementing a more rigorous adaptive time stepping method that uses ideas from spectral deferred correction methods [5, 10, 23]. At each time step, we estimate the local truncation error and then try to commit a constant amount of error per time step by adjusting the time step size. We leave the details and the implementation as future work. Future work also includes adaptivity in space. If vesicles are sufficiently far from one another, their hydrodynamic interaction can be represented with a moderate number of points, but as they approach one another, the hydrodynamic interaction strengthens and this requires a finer spatial resolution.

4. Computing Local Averages of Pressure and Stress

In many applications, we need to compute local averages of pressure and stress. The pressure p^S and stress T^S of the single-layer potential $\mathbf{u}(\mathbf{x}) = \mathcal{S}[\mathbf{f}](\mathbf{x})$ are

$$p^S(\mathbf{x}) = \sum_{q=1}^M p_q^S(\mathbf{x}) = \frac{1}{2\pi} \sum_{q=1}^M \int_{\gamma_q} \frac{\mathbf{r} \cdot \mathbf{f}_q}{\rho^2} ds,$$

and

$$T^S[\boldsymbol{\sigma}](\mathbf{x}) = \sum_{q=1}^M T_q^S[\boldsymbol{\sigma}](\mathbf{x}) = \frac{1}{\pi} \sum_{q=1}^M \int_{\gamma_q} \frac{\mathbf{r} \cdot \boldsymbol{\sigma} \mathbf{r}}{\rho^2} \frac{\mathbf{r} \otimes \mathbf{r}}{\rho^2} \mathbf{f}_q ds.$$

The pressure p^D and stress T^D of the double-layer potential $\mathbf{u}(\mathbf{x}) = \mathcal{D}[\mathbf{f}](\mathbf{x})$ are

$$p^D(\mathbf{x}) = \sum_{q=1}^M p_q^D(\mathbf{x}) = -\frac{1}{\pi} \sum_{q=1}^M \int_{\gamma_q} \frac{1}{\rho^2} \left(1 - 2 \frac{\mathbf{r} \otimes \mathbf{r}}{\rho^2} \right) \mathbf{n} \cdot \mathbf{f}_q ds,$$

³The streamlines of Stokes equations never intersect. Therefore, it is physically impossible for vesicles to collide with one another or with solid walls in finite time. Lubrication theory can be used to study the forces between nearly touching vesicles, and therefore compute estimates of the distance between the vesicles, but we choose not to discuss these forces here.

and

$$\begin{aligned}
T^D[\boldsymbol{\sigma}](\mathbf{x}) &= \sum_{q=1}^M T_q^D[\boldsymbol{\sigma}](\mathbf{x}) \\
&= \frac{1}{\pi} \sum_{q=1}^M \int_{\gamma_q} \left(\frac{\mathbf{n} \cdot \mathbf{f}_q}{\rho^2} \boldsymbol{\sigma} - \frac{8}{\rho^6} (\mathbf{r} \cdot \mathbf{n})(\mathbf{r} \cdot \mathbf{f}_q)(\mathbf{r} \cdot \boldsymbol{\sigma}) \mathbf{r} \right. \\
&\quad \left. + \frac{\mathbf{r} \cdot \mathbf{n}}{\rho^4} (\mathbf{r} \otimes \mathbf{f}_q + \mathbf{f}_q \otimes \mathbf{r}) \boldsymbol{\sigma} + \frac{\mathbf{r} \cdot \mathbf{f}_q}{\rho^4} (\mathbf{r} \otimes \mathbf{n} + \mathbf{n} \otimes \mathbf{r}) \boldsymbol{\sigma} \right) ds.
\end{aligned}$$

With these expressions, we can evaluate the pressure and stress tensor for bounded and unbounded flows with viscosity contrast. Moreover, computing the pressure of the single-layer potential can be accelerated with the standard Laplace FMM.

To evaluate the pressure and stress tensor near a vesicle, we again require near-singular integration. Since we require boundary values (see \mathbf{x}_0 in the left plot of Figure 1), formulas for the jumps in pressure and stress as a target point approaches a vesicle are required. The pressures p_q^S and p_q^D satisfy

$$\begin{aligned}
\lim_{\substack{\mathbf{x} \rightarrow \mathbf{x}_0 \\ \mathbf{x} \in \omega_q}} p_q^S(\mathbf{x}) &= \frac{\mathbf{f}_0 \cdot \mathbf{n}_0}{2} + p_q^S(\mathbf{x}_0), & \lim_{\substack{\mathbf{x} \rightarrow \mathbf{x}_0 \\ \mathbf{x} \notin \omega_q}} p_q^S(\mathbf{x}) &= -\frac{\mathbf{f}_0 \cdot \mathbf{n}_0}{2} + p_q^S(\mathbf{x}_0), \\
\lim_{\substack{\mathbf{x} \rightarrow \mathbf{x}_0 \\ \mathbf{x} \in \omega_q}} p_q^D(\mathbf{x}) &= -\frac{\partial \mathbf{f}_0}{\partial \boldsymbol{\tau}} \cdot \boldsymbol{\tau} + p_q^D(\mathbf{x}_0), & \lim_{\substack{\mathbf{x} \rightarrow \mathbf{x}_0 \\ \mathbf{x} \notin \omega_q}} p_q^D(\mathbf{x}) &= \frac{\partial \mathbf{f}_0}{\partial \boldsymbol{\tau}} \cdot \boldsymbol{\tau} + p_q^D(\mathbf{x}_0),
\end{aligned}$$

where $\mathbf{x}_0 \in \gamma$ and $\mathbf{f}_0 = \mathbf{f}(\mathbf{x}_0)$. The jumps for p_q^S are proved in Appendix B and the jumps for p_q^D are proved in [43]. To compute p_q^S and p_q^D at \mathbf{x}_0 , we use odd-even integration which has spectral accuracy if the singularity of the integrand at $\mathbf{x} = \mathbf{x}_0$ is no stronger than $(\mathbf{x} - \mathbf{x}_0)^{-1}$ [39]. Odd-even integration can be directly applied to evaluate $p_q^S(\mathbf{x}_0)$. However, as $\mathbf{x} \rightarrow \mathbf{x}_0$, the singularity of $p_q^D(\mathbf{x}_0)$ is of the order $(\mathbf{x} - \mathbf{x}_0)^{-2}$; therefore, we have to interpret the integral in the principal value sense. Since a constant hydrodynamic density \mathbf{f} results in the pressure vanishing [18, 27], we can reduce the strength of the singularity to $(\mathbf{x} - \mathbf{x}_0)^{-1}$ by first subtracting $\mathbf{f}(\mathbf{x}_0)$ and then evaluating $p_q^D(\mathbf{x}_0)$.

We do a convergence study on p^S and p^D exterior to the unit circle with the hydrodynamic density $\mathbf{f} = [\cos(\theta) \cos(\theta)]^T$. The exact pressures are calculated using the Residue Theorem. We check the relative maximum errors along the vertical line $x = 1.01$ (Table 2). Since $p^S, p^D \in C^\infty$, we achieve super-algebraic convergence when near-singular integration is not required. However, near-singular integration introduces an error described in Appendix A. Table 2 indicates a 5^{th} -order convergence rate which is consistent with the 6^{th} -degree Lagrange interpolant used to interpolate values on γ to \mathbf{x}_0 . Figure 2 shows contour plots of the pressure for an extensional flow with no viscosity contrast, as well as the pressure along the vertical line that passes exactly between the two vesicles. Not surprisingly, the pressure between the two vesicles is increasing as the inter-vesicle distance decreases.

	$N = 32$	$N = 64$	$N = 128$	$N = 256$	$N = 512$	$N = 1024$
Single-layer Potential	$8.22e - 04$	$4.05e - 05$	$1.23e - 06$	$2.53e - 08$	$2.03e - 10$	$1.83e - 14$
Double-layer Potential	$8.22e - 04$	$4.05e - 05$	$1.23e - 06$	$2.53e - 08$	$2.03e - 10$	$2.78e - 13$

Table 2: The maximum relative errors in the calculation of the pressures using near-singular integration along the line $x = 1.01$. The exact pressures are computed analytically using the Residue Theorem, and they differ by a multiplicative constant which explains the proximity of the errors. The slope of the line of best fit on a log-log scale is 5.5. For $N = 1024$, the near zone Ω_0 is empty. This explains the sharp drop in the errors.

We now compute the limiting values of the stress tensors $T^S[\boldsymbol{\sigma}]$ and $T^D[\boldsymbol{\sigma}]$. The limiting values of $T_q^S[\boldsymbol{\sigma}]$

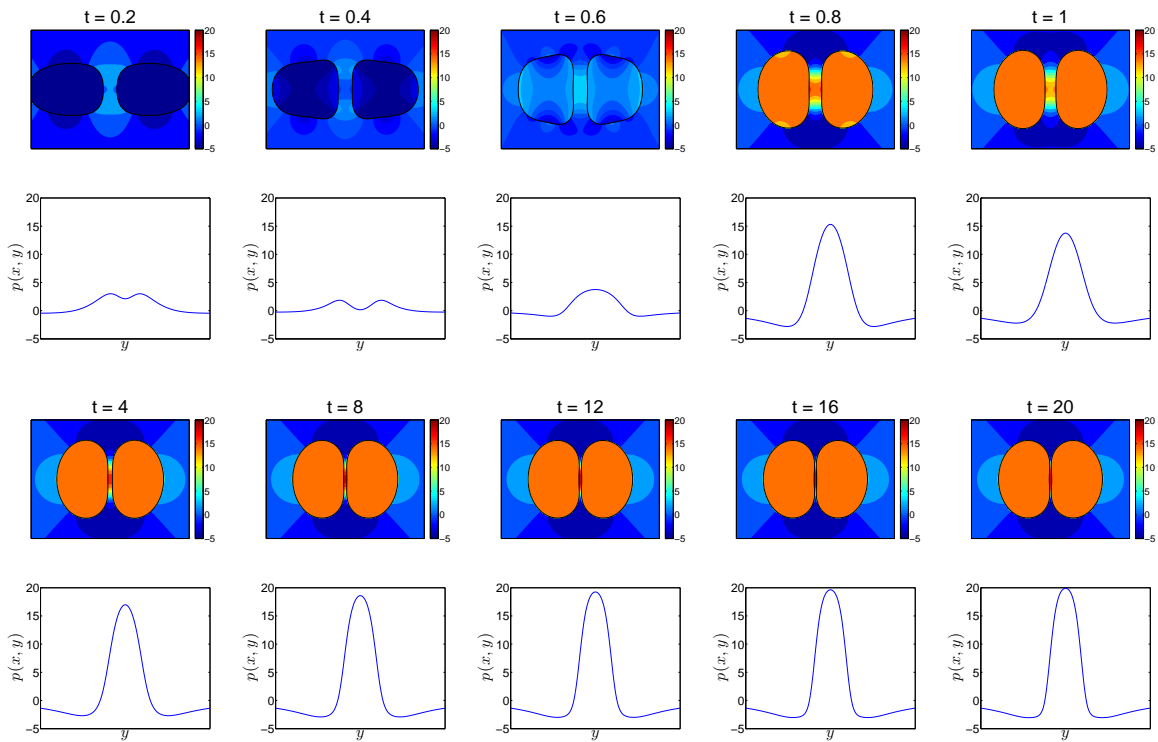


Figure 2: Contour plots show the pressure in and around the vesicles in an extensional flow with no viscosity contrast. The lower plots are the pressure along the vertical line that passes vertically through the midpoint of the two vesicles. We see that the maximum pressure increases as a function of time and that the pressure inside each vesicle approaches a constant value.

are

$$\lim_{\substack{\mathbf{x} \rightarrow \mathbf{x}_0 \\ \mathbf{x} \in \omega_q}} T_q^S[\boldsymbol{\sigma}](\mathbf{x}) = -\frac{1}{2}(\mathbf{n}_0 \otimes \mathbf{f}_0)\boldsymbol{\sigma}_0 + \frac{1}{2} \left(\boldsymbol{\tau} \otimes \begin{bmatrix} 2\tau_x\tau_y & \tau_y^2 - \tau_x^2 \\ \tau_y^2 - \tau_x^2 & -2\tau_x\tau_y \end{bmatrix} \mathbf{f}_0 \right) \boldsymbol{\sigma}_0 + T_q^S[\boldsymbol{\sigma}](\mathbf{x}_0), \quad (7)$$

$$\lim_{\substack{\mathbf{x} \rightarrow \mathbf{x}_0 \\ \mathbf{x} \notin \omega_q}} T_q^S[\boldsymbol{\sigma}](\mathbf{x}) = \frac{1}{2}(\mathbf{n}_0 \otimes \mathbf{f}_0)\boldsymbol{\sigma}_0 - \frac{1}{2} \left(\boldsymbol{\tau} \otimes \begin{bmatrix} 2\tau_x\tau_y & \tau_y^2 - \tau_x^2 \\ \tau_y^2 - \tau_x^2 & -2\tau_x\tau_y \end{bmatrix} \mathbf{f}_0 \right) \boldsymbol{\sigma}_0 + T_q^S[\boldsymbol{\sigma}](\mathbf{x}_0). \quad (8)$$

The jumps are proved in Appendix B. Since the singularity at $\mathbf{x} - \mathbf{x}_0$ is of the order $(\mathbf{x} - \mathbf{x}_0)^{-1}$, we use odd-even integration to compute the stress on γ_q . The jumps in the tensor of the double-layer potential are

$$\lim_{\substack{\mathbf{x} \rightarrow \mathbf{x}_0 \\ \mathbf{x} \in \omega_q}} T_q^D[\boldsymbol{\sigma}](\mathbf{x}) = -\frac{\partial \mathbf{f}_0}{\partial \boldsymbol{\tau}} \cdot \boldsymbol{\tau} \left(I + \begin{bmatrix} \tau_x^2 - \tau_y^2 & 2\tau_x\tau_y \\ 2\tau_x\tau_y & -\tau_x^2 + \tau_y^2 \end{bmatrix} \right) \boldsymbol{\sigma}_0 + T_q^D[\boldsymbol{\sigma}](\mathbf{x}_0),$$

$$\lim_{\substack{\mathbf{x} \rightarrow \mathbf{x}_0 \\ \mathbf{x} \notin \omega_q}} T_q^D[\boldsymbol{\sigma}](\mathbf{x}) = \frac{\partial \mathbf{f}_0}{\partial \boldsymbol{\tau}} \cdot \boldsymbol{\tau} \left(I + \begin{bmatrix} \tau_x^2 - \tau_y^2 & 2\tau_x\tau_y \\ 2\tau_x\tau_y & -\tau_x^2 + \tau_y^2 \end{bmatrix} \right) \boldsymbol{\sigma}_0 + T_q^D[\boldsymbol{\sigma}](\mathbf{x}_0).$$

These jumps are calculated using the jumps $\llbracket p^D \rrbracket$, $\llbracket \mathbf{u}^D \rrbracket$, $\llbracket T^D \mathbf{n} \rrbracket$, and $\llbracket \nabla \cdot \mathbf{u}^D \rrbracket$. We have already computed $\llbracket p^D \rrbracket$, and the other three jumps can be found in Appendix B of [43]. However, we have to use the same technique we used to compute $p^D(\mathbf{x}_0)$ to reduce the order of the singularity of the integral from $(\mathbf{x} - \mathbf{x}_0)^{-2}$ to $(\mathbf{x} - \mathbf{x}_0)^{-1}$. Since a constant hydrodynamic density \mathbf{f} corresponds to a vanishing stress tensor T^D , this modification guarantees that odd-even integration will converge to the correct value.

We check the convergence rate for the three components of the stress tensors (the (1, 2) and (2, 1) entries are identical). We use the same vesicle and hydrodynamic density as in Table 2. The maximum relative errors are in Table 3. Since $T^S, T^D \in C^\infty$, the errors in Table 3 are determined by the order of the near-singular integration algorithm. We obtain the expected 5th-order convergence.

		$N = 32$	$N = 64$	$N = 128$	$N = 256$	$N = 512$	$N = 1024$
Single-layer potential	(1, 1)	$8.33e-03$	$6.32e-04$	$2.40e-05$	$5.21e-07$	$4.30e-09$	$1.23e-14$
	(1, 2)	$5.79e-03$	$4.24e-04$	$1.59e-05$	$3.49e-07$	$2.89e-09$	$6.82e-15$
	(2, 2)	$4.39e-03$	$3.13e-04$	$1.15e-05$	$2.49e-07$	$2.05e-09$	$1.27e-14$
Double-layer potential	(1, 1)	$4.22e-03$	$3.34e-04$	$1.29e-05$	$2.81e-07$	$2.33e-09$	$1.12e-12$
	(1, 2)	$1.19e-02$	$8.98e-04$	$3.42e-05$	$7.54e-07$	$6.25e-09$	$1.75e-12$
	(2, 2)	$9.28e-03$	$6.80e-04$	$2.54e-05$	$5.50e-07$	$4.54e-09$	$5.36e-13$

Table 3: The maximum relative errors in the calculation of the stress tensor using near-singular integration along the line $x = 1.01$. The exact stress is computed analytically using the Residue Theorem. The convergence rates are all about 5.2. For $N = 1024$, the near zone Ω_0 is empty. This explains the sharp drop in the errors.

5. Results

We discuss the behaviour of the different time integrators for several bounded and unbounded vesicle suspensions. Because of the incompressibility of the fluid and the inextensibility of the vesicles, the area enclosed by a vesicle and its total length remain fixed. However, due to numerical errors, these quantities change throughout simulations. Penalty methods are often used to enforce maintain the vesicles length, but these techniques change the physics of the problem. In our formulation, no such penalty method is used and the inextensibility constraint is enforced algebraically using (3b). Even though the length and area of the vesicles are low-order moments of the shape, we have experimentally found that they are good estimates for the error of our numerical methods. Therefore, we use the relative errors in area and length to study the convergence rates of our different time integrators. We also report minimum distances between vesicles and solid walls to demonstrate convergence, but without an exact solution, we must use an over-refined solution as the exact solution. The experiments we perform are now summarized.

- **Shear Flow** (Tables 4–5 and Figure 3): Here we consider the classic problem of two vesicles in the shear flow $\mathbf{u} = (y, 0)$ with the left vesicle slightly elevated from the right vesicle. We study the effect of the reduced area and the viscosity contrast on the dynamics. Then, we compare the three different stable time integrators we have discussed: first-order with explicit and semi-implicit inter-vesicle interactions and second-order with semi-implicit inter-vesicle interactions. All three methods converge at the expected rate. Moreover, if we use first-order time stepping, semi-implicit and explicit inter-vesicle interactions give similar errors. Therefore, for first-order time stepping, if the time step is small enough, using explicit inter-vesicle interactions is appropriate since the resulting linear system is easier to solve.
- **Taylor-Green Flow** (Table 6 and Figures 4–5): Here we look at the stability of the semi-implicit inter-vesicle interactions. For a short time horizon, we quantify its stability. We do a convergence study and also discuss a significant difference in the behaviour of the first- and second-order time integrators.
- **Extensional Flow** (Table 7 and Figure 6): We consider two vesicles placed symmetrically in an extensional flow. We show that the simulation is unstable without near-singular integration. A convergence study shows that we achieve the desired first- and second-order convergence. We also report CPU times to demonstrate that we are achieving the expected complexity.
- **Stenosis** (Table 8–9 and Figure 7): We consider a single vesicle passing through a constriction in a confined flow. We are able to take a vesicle that is over two times taller than a similar simulation in [33]. A convergence study on the errors in area and length as well as the minimum distance between the vesicle and solid wall show that we achieve second-order accuracy.
- **Couette Apparatus** (Figures 8–9): High concentration flows are demonstrated with two Couette simulations, one with a moderate volume fraction and one with a high volume fraction. We compare first- and second-order time stepping with the moderate volume fraction and observe a similar behaviour in the errors that is described in the Taylor-Green example. For the larger volume fraction, we report results for first- and second-order time stepping which both require semi-implicit inter-vesicle interactions for the chosen time step size to be stable.

Other details of our results include:

- The parameters we investigate are the number of points per vesicle, N , the number of vesicles, M , the number of points per solid wall, N_{wall} , the time step size, Δt , the viscosity contrast, ν , and the time integrator.
- An important dimensionless quantity is the vesicle’s reduced area: the ratio of its area to the area of a circle of the same perimeter. Because of the incompressibility and inextensibility constraints, the reduced area should remain constant. Intuitively, the reduced area indicates how much the vesicle can deform. The closer the reduced area is to its maximum value of one, the less it is able to deform. We are particularly interested in vesicles of reduced area 0.65. This value results in shapes that resemble (two-dimensional approximations of) red blood cells.
- All vesicle-to-vesicle and vesicle-to-wall interactions are accelerated with the FMM. The wall-to-wall iterations are precomputed and stored and the wall-to-vesicle interactions are computed with the direct method which results in a $\mathcal{O}(MNN_{\text{wall}})$ calculation. For flows with viscosity contrast, the double-layer potential is also evaluated with the direct method resulting in a $\mathcal{O}(M^2N^2)$ calculation. Fast algorithms for these interactions are under consideration.
- We precondition all the linear systems with the block-diagonal preconditioner. We have observed that this results in a mesh-independent solver with semi-implicit interactions.
- We have experimented with different GMRES tolerances. If it is too large, second-order convergence is difficult to achieve. If it is too small, the condition number of the block-diagonal preconditioner makes the tolerance unachievable. Experimentally we have found that 10^{-12} is a good compromise.

- The bending modulus sets the time scale. We let $\kappa_b = 0.1$ for all simulations.
- All simulations are preformed in MATLAB on a six-core 2.67GHz Intel Xeon processor with 24GB of memory.

Estimation of the overall complexity. Here we summarize the cost of the most expensive parts of the overall algorithm. Recall that we are using a mesh-independent preconditioned GMRES iteration. Therefore, the cost can be summarized by the time required to preform one matrix-vector product.

- *Vesicle-vesicle interactions:* Using the FMM, the single-layer potential requires $\mathcal{O}(MN)$ operations.
- *Viscosity contrast:* Since we do not have a fast algorithm to compute the double-layer potential, viscosity contrast requires $\mathcal{O}(M^2N^2)$ operations. However, this is just a shortcoming of the specific implementation, not a theoretical one.
- *Confined flows:* Wall-to-wall interactions are precomputed and stored. Wall-to-vesicle interactions require $\mathcal{O}(MNN_{\text{wall}})$ operations and vesicle-to-wall interactions require $\mathcal{O}(MN + N_{\text{wall}})$ operations using the FMM.
- *Near-singular integration:* Our near-singular integration complexity is summarized in Section 3.4. The upsampling results in an increase in the above complexities. For instance, vesicle-vesicle interactions with the FMM require $\mathcal{O}(MN^{3/2} + MN)$ operations and vesicle-to-wall interactions require $\mathcal{O}(MN^{3/2} + N_{\text{wall}})$. However, since we have not implemented a fast summation for the double-layer potential, flows with a viscosity contrast require a $\mathcal{O}(M^2N^{5/2})$ calculation.

5.1. Shear Flow

Here we consider two vesicles in the shear flow $(y, 0)$. We initially place the left vesicle's center slightly above the x-axis and place the right vesicle's center exactly on the x-axis. Initially, we expect the right vesicle to undergo tank-treading [12, 24] while the other vesicle will travel from left to right. Here we study the effect of the reduced area and the viscosity contrast on the dynamics and errors. We expect vesicles with larger viscosity contrast and larger reduced areas to behave more like rigid bodies. In particular, we expect them to come closer to one another. Figure 3 indicate that a higher viscosity contrast results in the vesicles coming closer together. Moreover, for larger reduced areas, the effect of the viscosity contrast is less pronounced. We also see that vesicles with a larger reduced area come closer together.

We now do a convergence study for both values of the reduced area and viscosity contrast. We vary the number of points per vesicle, the number of time steps, and the time integrator. We report the errors in area and length at the time horizon $t = 12$ in Tables 4 and 5. First, we see that first- and second-order convergence is achieved for all combinations of reduced area and viscosity contrast. Second, semi-implicit inter-vesicle interactions do not improve the accuracy of first-order time stepping, but, we will see later that this time integrator is more stable.

5.2. Taylor-Green Flow

We consider the Taylor-Green flow $\mathbf{u} = (\sin x \cos y, -\cos x \sin y)$ with 9 vesicles each with $N = 64$ points of reduced area 0.65 placed inside the periodic cell $(0, 2\pi)^2$ (left plot of Figure 4). We consider first-order IMEX Euler with both semi-implicit and explicit inter-vesicle interactions. We find the largest time step of both methods so that the vesicles do not cross before a time horizon of $T = 1$. With explicit interactions, the vesicles cross if 74 time steps are taken but not if 75 time steps are taken. However, with semi-implicit interactions, the simulation successfully completes even with one time step. Of course the error is too large and a time step size this large is unreasonable.

For this example, we found that using explicit interactions with 75 time steps requires approximately the same amount of CPU time as using semi-implicit interactions with 30 time steps. Therefore, if one permits the error to be approximately 2.5 times larger, using semi-implicit inter-vesicle interactions is justified.

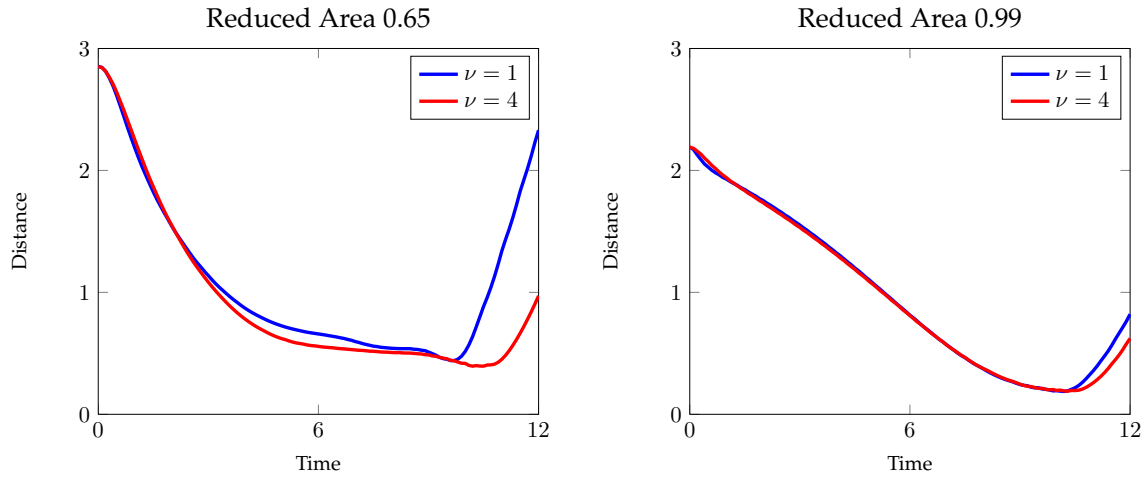
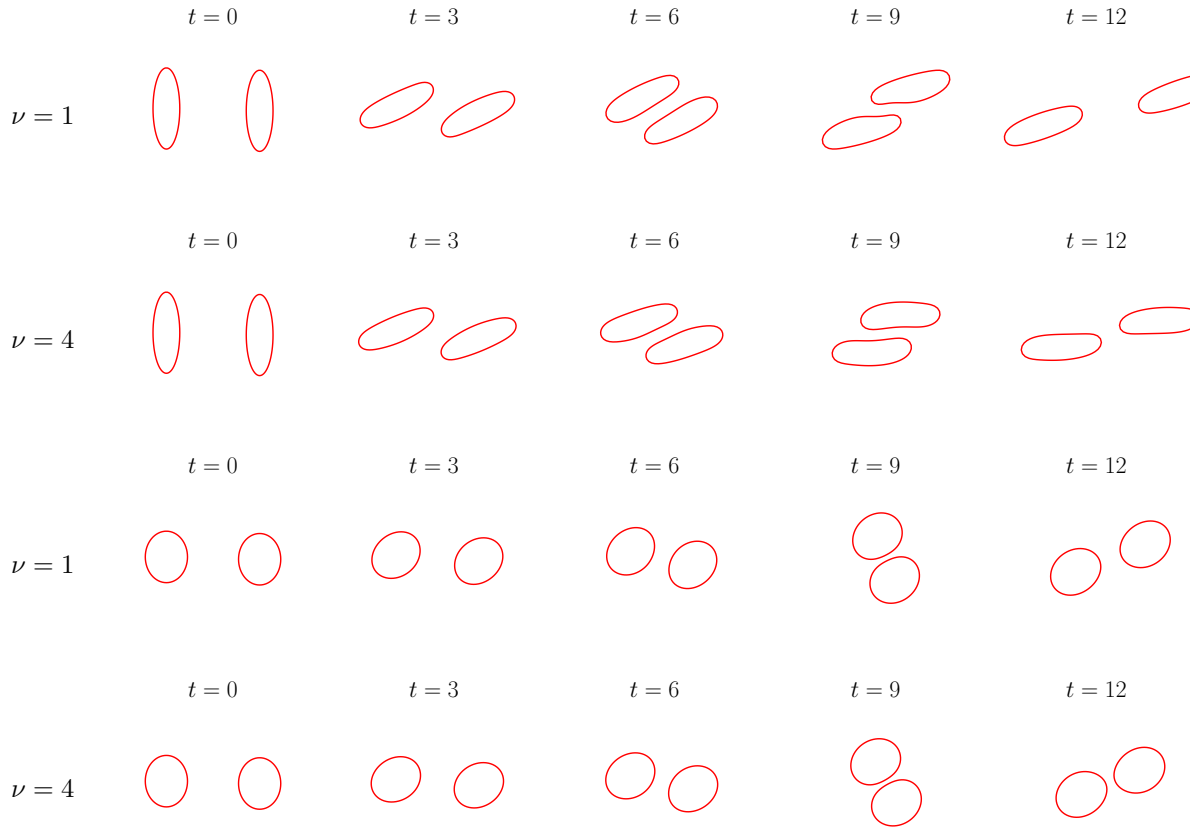


Figure 3: Two vesicles are submerged in a shear flow. In the first and second rows, the vesicles have reduced area 0.65, and in the third and fourth rows, the vesicles have reduced area 0.99. Each simulation is done with viscosity contrasts $\nu = 1$ and $\nu = 4$. The bottom plots show the distance between the vesicles for both reduced areas and both viscosity contrasts. Comparing semi-implicit inter-vesicle interactions with both first- and second-order time stepping, the distance between the vesicles never differ by more than 2.2% for both reduced areas and both viscosity contrasts.

Time Integrator	N	Δt	$\nu = 1$		$\nu = 4$	
			e_A	e_L	e_A	e_L
Explicit (1)	32	0.04	$6.73e-2$	$5.21e-2$	$4.07e-2$	$2.41e-2$
Explicit (1)	64	0.02	$3.36e-2$	$2.62e-2$	$2.02e-2$	$1.20e-2$
Explicit (1)	128	0.01	$1.68e-2$	$1.31e-2$	$1.01e-2$	$5.99e-2$
Implicit (1)	32	0.04	$6.73e-2$	$5.21e-2$	$4.06e-2$	$2.40e-2$
Implicit (1)	64	0.02	$3.36e-2$	$2.62e-2$	$2.02e-2$	$1.20e-2$
Implicit (1)	128	0.01	$1.68e-2$	$1.31e-2$	$1.02e-2$	$5.98e-3$
Implicit (2)	32	0.04	$1.59e-4$	$3.21e-4$	$2.69e-5$	$6.33e-5$
Implicit (2)	64	0.02	$3.87e-6$	$6.52e-5$	$3.78e-6$	$1.20e-5$
Implicit (2)	128	0.01	$2.79e-7$	$1.47e-5$	$3.85e-7$	$2.28e-6$

Table 4: The errors in area and length at $t = 12$ for different time integrators applied to two vesicles of reduced area 0.65 in a shear flow. The parenthetic values are the time stepping order. Results are presented for no viscosity contrast and a viscosity contrast of 4.

Time Integrator	N	Δt	$\nu = 1$		$\nu = 4$	
			e_A	e_L	e_A	e_L
Explicit (1)	32	0.04	$1.05e-1$	$5.48e-2$	$9.67e-2$	$4.94e-2$
Explicit (1)	64	0.02	$5.15e-2$	$2.70e-2$	$4.78e-2$	$2.45e-2$
Explicit (1)	128	0.01	$2.55e-2$	$1.34e-2$	$2.37e-2$	$1.22e-2$
Implicit (1)	32	0.04	$1.05e-1$	$5.48e-2$	$9.69e-2$	$4.93e-2$
Implicit (1)	64	0.02	$5.16e-2$	$2.70e-2$	$4.77e-2$	$2.45e-2$
Implicit (1)	128	0.01	$2.55e-2$	$1.34e-2$	$2.36e-2$	$1.22e-2$
Implicit (2)	32	0.04	$2.40e-5$	$1.13e-4$	$5.85e-5$	$4.68e-5$
Implicit (2)	64	0.02	$1.65e-6$	$1.50e-5$	$7.05e-6$	$5.86e-6$
Implicit (2)	128	0.01	$1.56e-7$	$1.92e-6$	$8.62e-7$	$7.26e-7$

Table 5: The errors in area and length at $t = 12$ for different time integrators applied to two vesicles of reduced area 0.99 in a shear flow. The parenthetic values are the time stepping order. Results are presented for no viscosity contrast and a viscosity contrast of 4.

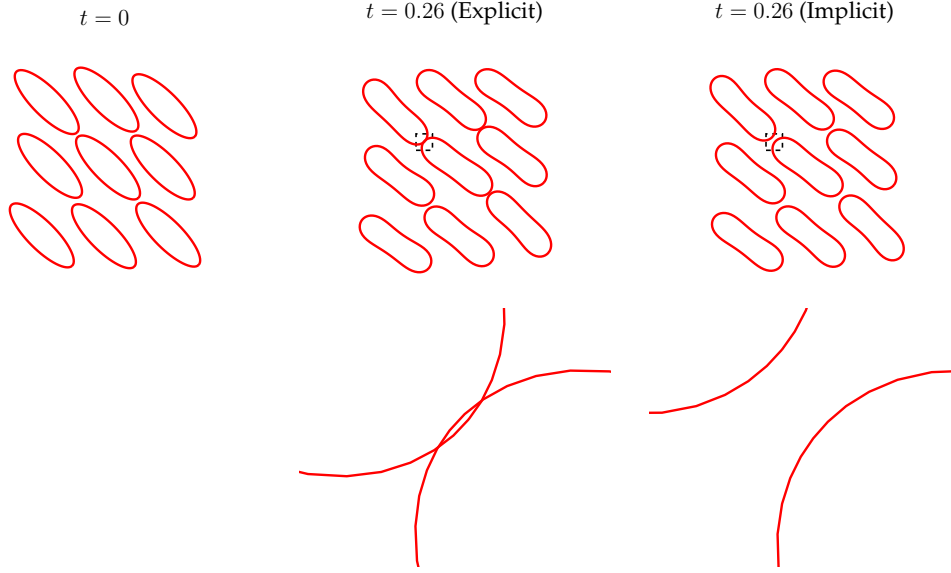


Figure 4: We compare first-order time stepping with explicit and semi-implicit inter-vesicle interactions for a time step size of 0.02 and 64 points per vesicle with the initial configuration in the left-most plot. With explicit interactions (middle plot), the vesicles cross after only 13 time steps. However, with semi-implicit interactions (right plot), the vesicles do not cross. The bottom plots show magnifications of the region where the explicit solver first crosses.

We do a convergence study for first- and second-order time stepping with semi-implicit inter-vesicle interactions. If these interactions are treated explicitly, the coarsest simulation results in the vesicles crossing. We achieve the desired first-order convergence, but second-order convergence is not achieved at these resolutions. However, we ran the simulation with $\Delta t = 3.13e - 4$ and $\Delta t = 1.56e - 4$ and this is where second-order convergence is first observed; the error in area reduced by 4.67 and the error in length reduced by 3.96.

We have also observed a qualitative difference in the behaviour of the errors of first- and second-order time stepping. The errors of the first-order methods continue to grow throughout the simulation, while for second-order time stepping, the errors plateau. Thus, given a fixed time step size, second-order time stepping can simulate longer time horizons than first-order time stepping. We demonstrate this behaviour in the bottom plot of Figure 5 where we plot the errors in area and length for the first- and second-order time stepping. Snapshots of the simulation are in the top plots of Figure 5.

N	Δt	First-order		Second-order	
		e_A	e_L	e_A	e_L
32	$2e - 2$	$5.24e - 2$	$3.03e - 2$	$5.25e - 4$	$3.98e - 3$
64	$1e - 2$	$2.77e - 2$	$1.64e - 2$	$2.08e - 4$	$1.96e - 3$
128	$5e - 3$	$1.43e - 2$	$8.68e - 3$	$7.76e - 5$	$9.42e - 4$
256	$2.5e - 3$	$7.24e - 3$	$4.53e - 3$	$2.73e - 5$	$4.20e - 4$

Table 6: The errors in area and length at $t = 5$ for a Taylor-Green flow. All runs were done with semi-implicit inter-vesicle interactions since explicit interactions with $N = 32$ and $\Delta t = 2e - 2$ results in crossing vesicles.

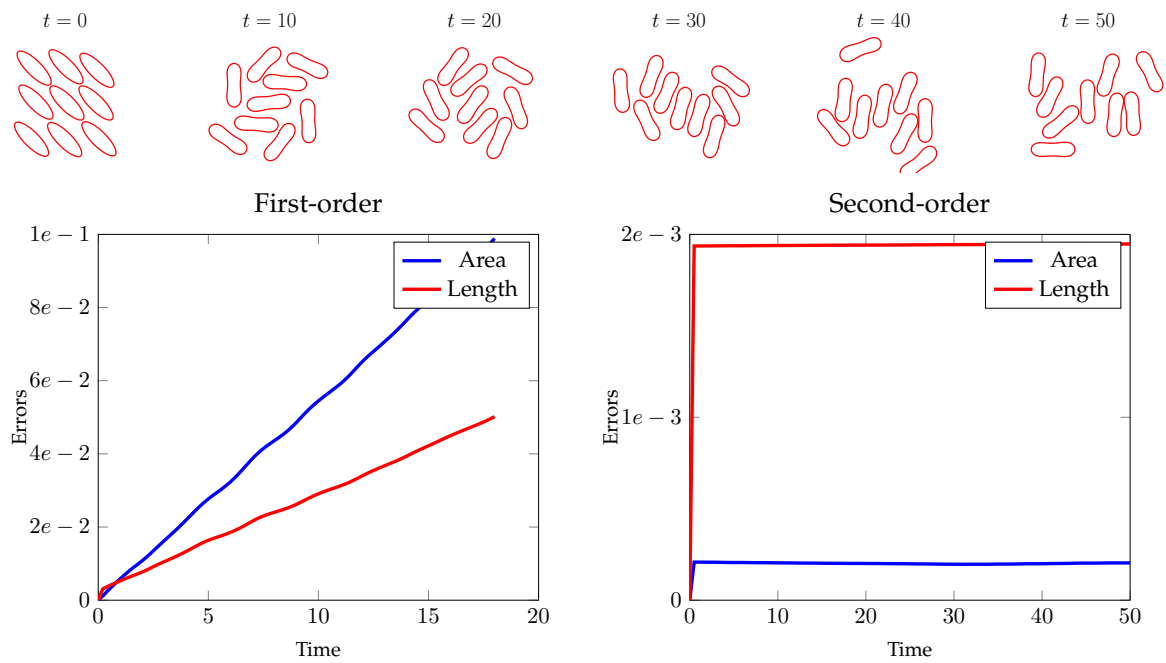


Figure 5: The top plots show several snapshots of a Taylor-Green simulation with a long time horizon using second-order time stepping. In the bottom plots are the errors in area and length for the first- and the second-order time integrators. Notice that the errors for the first-order method continue to grow and the simulation stops near $t = 20$ (the simulation is stopped when a 10% error has been incurred), whereas the errors for the second-order method plateau and the simulation is able to run much longer.

5.3. Extensional Flow

We consider two vesicles with reduced area 0.65 symmetrically placed around the origin (top plots of Figure 6). The background velocity is given by $\mathbf{u} = (-x, y)$. We first run the simulation with and without near-singular integration. We compute the distance between the vesicles, and the errors in area and length (bottom plots of Figure 6). We see that when $t \approx 5$, the simulation without near-singular integration begins to introduce large errors in the area of the vesicles. This indicates that the approximation of the single-layer potential is not adequate. Then, around $t \approx 12$, the vesicles are too close for the N -point trapezoid rule and the simulations fails. This agrees with our error estimate from Appendix A since for this simulation, an arclength term is approximately 0.24. However, with near-singular integration, the simulation successfully runs to completion.

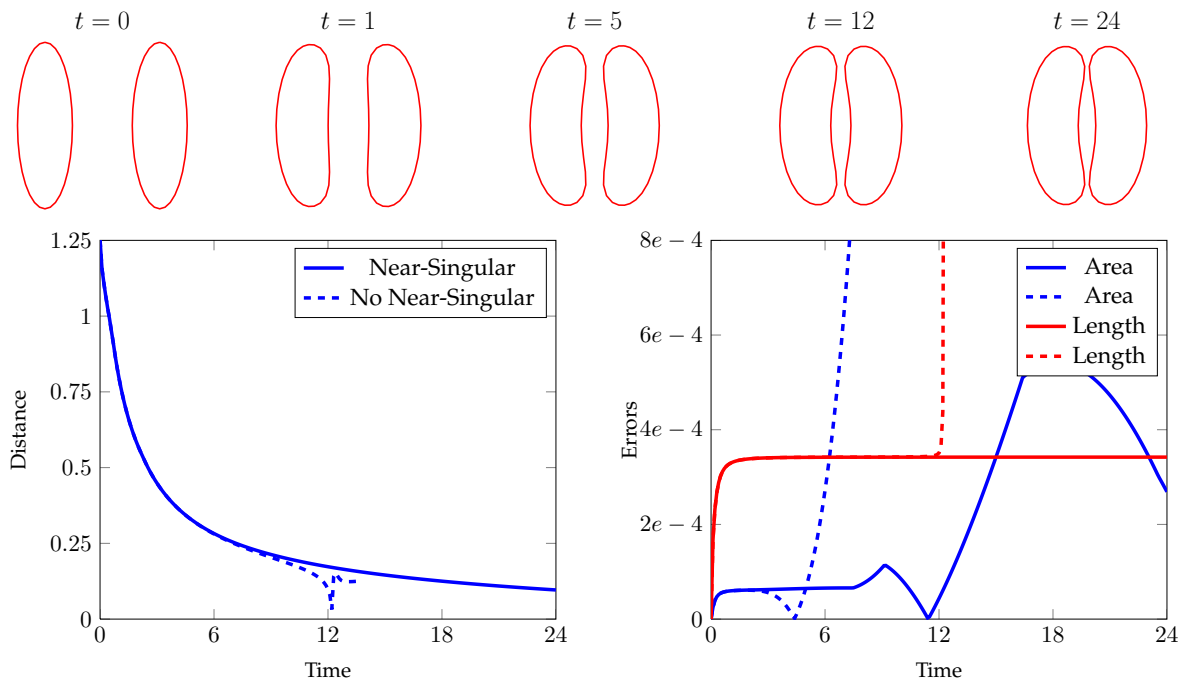


Figure 6: Top: Two vesicles discretized with $N = 32$ points at several time steps using near-singular integration. Bottom left: The distance between the two vesicles both with (solid) and without (dashed) near-singular integration. Bottom right: The error in area (blue) and length (red) with (solid) and without (dashed) near-singular integration.

We report the errors in area and length at $t = 24$ in Table 7. Also reported is the error in the distance between the vesicles at $t = 24$, for which we take the “true” distance from an overrefined simulation. As before, we achieve first-order convergence and there is little difference between the accuracy when comparing explicit and semi-implicit inter-vesicle interactions. We also achieve second-order convergence, but it requires a finer time step size when compared to the first-order methods before the asymptotic rate is achieved.

In Table 7, we also list the required CPU time per time step relative to the smallest simulation. When the number of points is doubled from 32 to 64, the amount of work per time step goes up by less than a factor of two. The increase in CPU time when N is doubled from 64 to 128 is attributed to extra work required by near-singular integration since, to simplify the implementation, we only work with powers of 2. Therefore, we upsample 64 to 256, but 128 is upsampled to 4096. We also see that semi-implicit inter-vesicle interactions are computationally not much more expensive. This is because a lot of work is spent precomputing the block-diagonal preconditioner which is done once per time step for all the time integrators.

Integrator	N	Δt	e_A	e_L	e_{gap}	CPU Time
Explicit (1)	32	0.04	$1.99e-4$	$6.53e-4$	$1.97e-1$	—
Explicit (1)	64	0.02	$6.34e-5$	$3.42e-4$	$3.73e-3$	1.15
Explicit (1)	128	0.01	$3.13e-5$	$1.78e-4$	$1.16e-3$	2.83
Implicit (1)	32	0.04	$2.12e-4$	$6.64e-4$	$1.92e-1$	2.65
Implicit (1)	64	0.02	$6.43e-5$	$3.46e-4$	$2.23e-3$	2.72
Implicit (1)	128	0.01	$3.15e-5$	$1.79e-4$	$4.35e-4$	7.40
Implicit (2)	32	0.04	$3.26e-4$	$1.38e-4$	$3.96e-2$	2.43
Implicit (2)	64	0.02	$4.14e-6$	$4.45e-5$	$8.32e-2$	2.89
Implicit (2)	128	0.01	$5.08e-7$	$1.27e-5$	$2.69e-2$	8.13
Implicit (2)	128	0.005	$1.02e-7$	$3.13e-6$	$1.27e-4$	7.70

Table 7: The errors in area, length, and the error in the gap size at $t = 24$, and the CPU time per time step for the extensional flow. The parenthesis values are the order of the time integrator. The error in the gap size is found by computing a “true” solution with $N = 256$ points per vesicle and a time step size so that the error in area is $9.0e-9$ and in length is $7.3e-11$. The CPU times are relative to the simulation with $N = 32$, $\Delta t = 0.04$ which took approximately $2.62e-1$ seconds per time step.

5.4. Stenosis

We consider a single vesicle of reduced area 0.65 in a constricted tube. The solid wall is parameterized as $\mathbf{x}(\theta) = 10r(\theta) \cos(\theta)$ and $y(\theta) = 3r(\theta) \sin(\theta)\eta(\theta)$, where $r(\theta) = (\cos(\theta)^8 + \sin(\theta)^8)^{-1/8}$, and

$$\eta(\theta) = \begin{cases} \frac{1-0.6 \cos(x)}{1.6} & |x(\theta)| \leq \pi, \\ 1 & |x(\theta)| > \pi. \end{cases}$$

For this geometry, the error of the trapezoid rule is $\mathcal{O}(10^{-4})$ with $N_{\text{wall}} = 256$ points and is $\mathcal{O}(10^{-6})$ with $N_{\text{wall}} = 512$ points. We impose a Gaussian-shaped boundary condition at the intake and outake of the tube which is plotted along with the geometry in Figure 7. The vesicle’s initial height is 2.3 times larger than the size of the constriction. We report a convergence study for second-order time stepping in Table 8 and we exceed the expected rate of convergence. We note that for this example, N_{wall} can not be less than 256. If it is, the Lagrange interpolation points required by near-singular integration for wall-to-vesicle interactions are on both sides of the solid wall. Since the double-layer potential has a jump across the solid wall, this creates a discontinuity in the velocity field and the method becomes unstable.

This example is ideally situated for adaptive time stepping. As the vesicle passes through the constriction, large jumps in the errors are committed. In the simulation with $\Delta t = 5.0e-3$, the error in length jumps by four orders of magnitude, and the error in area jumps by three orders of magnitude near $t = 3$. These jumps are less severe in the simulation with $\Delta t = 2.5e-3$, which has a jump of one order of magnitude in length and two orders of magnitude in area.

N	N_{wall}	Δt	e_A	e_L
128	256	$5.0e-3$	$6.55e-4$	$1.17e-2$
256	512	$2.5e-3$	$9.59e-7$	$1.05e-6$

Table 8: The errors in area and length at $t = 8$ for the second-order stenosis flow.

We also report the minimum distance, and the time when the minimum distance occurs, between the vesicle and the solid wall in Table 9. In order to focus the error on the time step size, we take a fine spatial resolution of $N = 256$ and $N_{\text{wall}} = 512$. We report the minimum over time of the distance

$$d(\gamma, \Gamma) = \inf_{\mathbf{x} \in \gamma, \mathbf{y} \in \Gamma} \|\mathbf{x} - \mathbf{y}\|$$

rather than the error since an exact solution is not available. The time integrators predict different locations, t_{min} , where the minimum occurs, but they both are converging. For the first-order results, if we compare

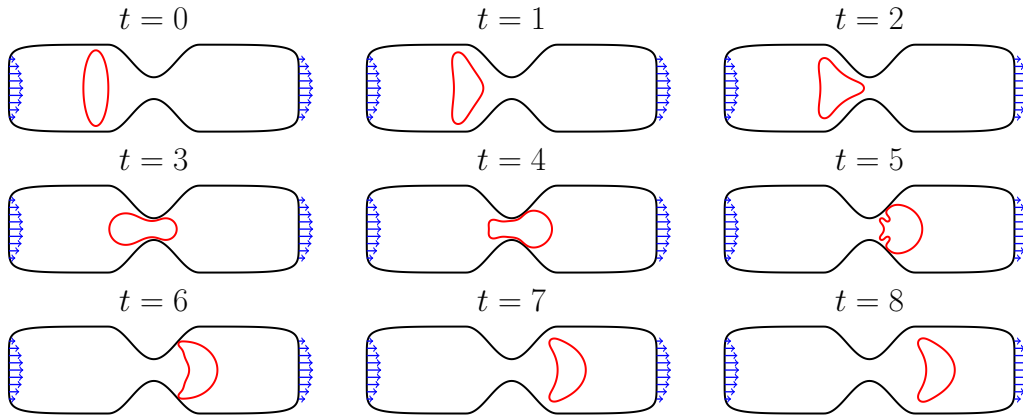


Figure 7: Snapshots of a single vesicle in a constricted tube. The boundary condition on the solid wall (plotted in blue) at the inlet and outlet is Gaussian-shaped, and on the remainder of the solid wall is zero. The vesicle is initially 2.3 times larger than the size of the constriction. Results from [33] were only able to simulate vesicles that were 1.12 times larger than the constriction.

the minimum distances with the distance of the most accurate second-order simulation at $t = 5.26$, which is $9.6369e - 2$, then we see that first-order convergence has been achieved. Without a much more accurate numerical solution, we are unable to compute convergence rates for the second-order results. However, it appears that we have resolved the distance up to at least three digits of accuracy.

Δt	First-order		Second-order	
	t_{\min}	$d(\Gamma, \gamma)$	t_{\min}	$d(\Gamma, \gamma)$
$1.0e - 2$	4.37	$1.0318e - 1$	4.34	$1.0196e - 1$
$5.0e - 3$	4.41	$1.0262e - 1$	4.39	$9.8055e - 2$
$2.5e - 3$	4.42	$1.0143e - 1$	5.77	$9.5809e - 2$
$1.3e - 3$	5.26	$9.9541e - 2$	5.77	$9.5804e - 2$
$6.3e - 4$	5.26	$9.7938e - 2$	5.77	$9.5803e - 2$
$3.1e - 4$	5.26	$9.7137e - 2$	5.77	$9.5802e - 2$

Table 9: The minimum distance, $d(\Gamma, \gamma)$, between the vesicle and the solid wall, and the time, t_{\min} , when this distance is achieved. Rather than forming an overrefined "true" solution, we report the actual distances.

5.5. Couette Apparatus

Here we consider two simulations of a Couette apparatus with different volume fractions. We first consider a Couette apparatus where the inner boundary, which is slightly off-centered, is rotating with constant angular velocity and the outer boundary is fixed. We randomly place 42 vesicles of reduced area 0.65 inside the apparatus which corresponds to a volume fraction of 20%. Each vesicle is discretized with 64 points, each solid wall with 64 points, the time step size is 0.01, and the time horizon is $T = 30$. Snapshots of the simulation are in the top plots of Figure 8. Using first-order time stepping with explicit inter-vesicle interactions, the error in area is $1.70e - 2$ and the error in length is $7.94e - 2$ at $t = 30$. Semi-implicit inter-vesicle interactions are not required for this time step size. The simulation took a little less than 6 hours, or about 7.1 seconds per time step.

We repeat this experiment with second-order time stepping which requires semi-implicit inter-vesicle interactions. The simulation took about 83 hours, or about 100 seconds per time step. The errors in area and length at $t = 30$ are $2.95e - 3$ and $7.13e - 4$. To achieve a similar accuracy with first-order time stepping, a time step size 11 times smaller would be required which would require more than 83 hours of CPU time due to the double-layer potentials. Moreover, the errors in area and length for second-order time stepping

have plateaued while for first-order time stepping, they continue to grow (bottom plots of Figure 8). Again, this means that with second-order time stepping, we can take much longer time horizons without requiring a smaller time step size.

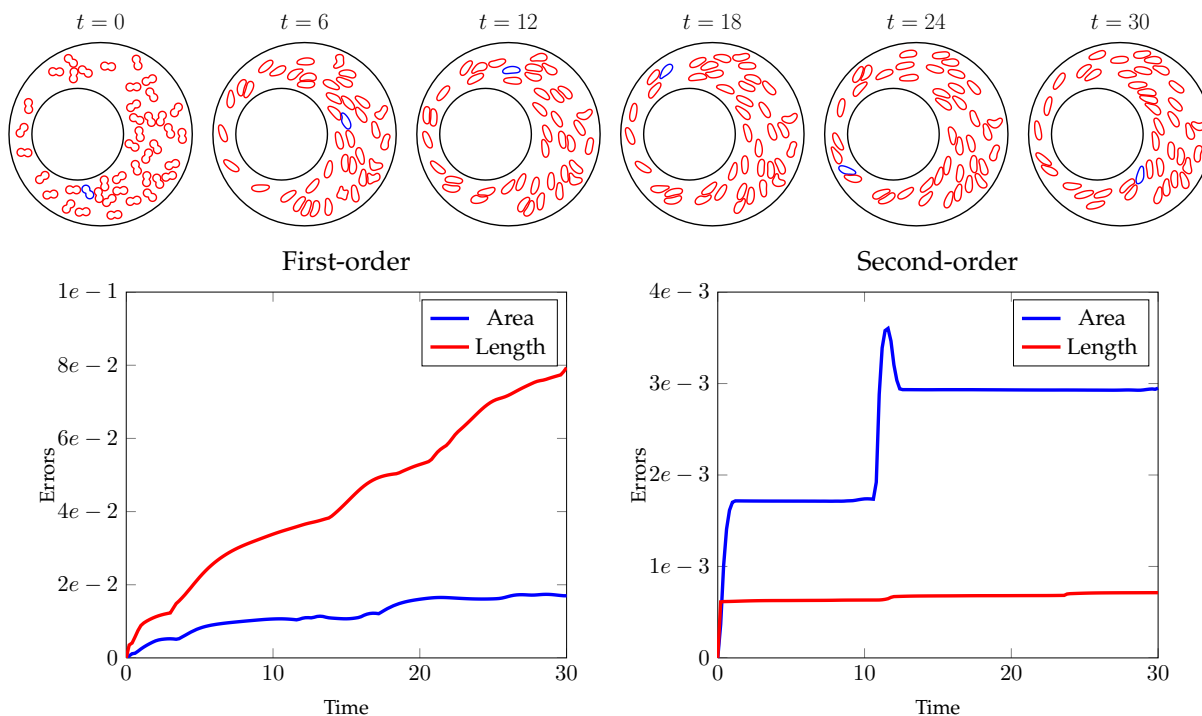


Figure 8: The top plots show snapshots of a Couette flow with 42 vesicles and a volume fraction of 20%. One vesicle is coloured in blue to view its time history. The outer boundary is fixed while the inner boundary completes one revolution every 10 time units. The bottom plots show the errors in area and length for the first- and second-order time integrators. Notice that the errors for first-order method continue to grow whereas the errors for the second-order method plateau.

We now consider a Couette apparatus with the inner boundary exactly in the middle of the outer boundary. We use 150 vesicles of reduced area 0.65 resulting in a volume fraction of approximately 40.5%. With this higher concentration, a finer discretization of the solid walls is required to resolve its density function η . Therefore, we have discretized both boundaries with 256 points. We also used our collision detection algorithm to alert us if vesicles had crossed. With $\Delta t = 0.01$ and explicit inter-vesicle interactions, the first-order method results in crossing vesicles. Therefore, we report the results using first-order semi-implicit inter-vesicle interactions which does not result in vesicles crossing. Snapshots are illustrated in Figure 9. On average, each time step required 27 GMRES iterations. The total simulation took about 10 days, but this number will drop dramatically once the double-layer potential is implemented with a fast summation method. At $t = 10$, the error in area is $9.62e - 3$ and the error in length is $1.92e - 2$. We also ran this simulation with second-order time stepping and achieved an error in area of $9.39e - 4$ and an error in length of $4.19e - 4$.

6. Conclusions

We have presented and tested a collection of extensions of the boundary integral equation formulation for vesicle suspensions outlined in [33]. Our goal is to create a robust method for handling high concentration suspensions. The main contributions we have presented are:

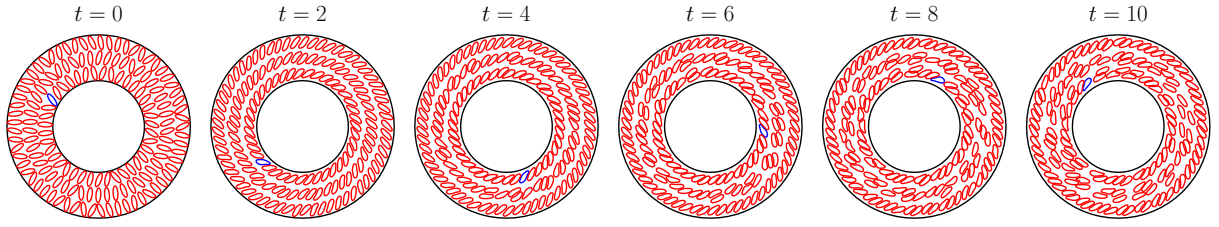


Figure 9: Snapshots of a Couette flow with 150 vesicles. One vesicle is coloured in blue to view its time history. The inner boundary completes one full revolution every 10 time units.

- To remove stiffness, we have introduced a new time integrator that treats inter-vesicle interactions semi-implicitly. This allows us to take larger time steps and to use second-order time stepping.
- To handle vesicles in close proximity, we employed and tested the near-singular integration algorithm outlined in [43]. This algorithm creates a uniform error when evaluating integral operators, is easy to implement, and does not significantly increase the overall complexity. The vesicle flow configurations that we tested are unstable without near-singular integration.
- To test for collisions, we introduced a spectrally accurate algorithm that uses standard potential theory and is compatible with our near-singular integration scheme and the fast multipole method.
- We computed the pressure and stress of the single- and double-layer potentials. To use near-singular integration, we require the limiting values of the pressure and stress as the target point approaches the boundary. All these jumps were computed.
- We obtained first- and second-order convergence for a variety of bounded and unbounded flows. We also observed examples where the errors for second-order convergence plateau while the error for first-order convergence continues to grow.

While these contributions are a major step towards creating a robust solver for high concentration vesicle suspensions, there are several key features that are necessary and are currently being investigated.

- The vesicle shapes we have presented in Section 5 can be well represented with $N = 128$ or fewer points per vesicle. However, we may require more points to represent quantities such as the traction jump or the velocity field. Therefore, spatial adaptivity is under consideration.
- Currently, the time step is found using a trial and error process. We are developing high-order time integrators that use error control to automatically and adaptively adjust the time step size.
- Our formulation is two-dimensional. The algorithms we have introduced naturally extend to three-dimensions, but the linear systems are far too expensive to solve without suitable preconditioners.
- Our formulation uses the steady Stokes equations for both the fluid in the bulk and in the vesicle interior. If transient, inertial, or viscoelastic effects are important one has to use a different formulation.

A. Error estimates for near-singular integration

We compute error bounds for the near-singular integration scheme to justify our choice of the $N^{3/2}$ -point trapezoid rule for points in the far zone. Recall that the far zone is defined as all points that are more than distance h from a vesicle. Consider a vesicle with boundary $\gamma \in C^\infty$ and a density function $\mathbf{f} \in C^M$. Recall that the single-layer potential is

$$\mathbf{u}(\mathbf{x}) = \frac{1}{4\pi} \int_{\gamma} \left(-\log \rho + \frac{\mathbf{r} \otimes \mathbf{r}}{\rho^2} \right) \mathbf{f}(\mathbf{y}) ds_{\mathbf{y}}.$$

Following [43], we need to bound the derivatives of the kernel. Bounding the derivatives of the logarithm term is immediate, and the derivatives of the second term are bounded by noting that

$$\frac{\mathbf{r} \otimes \mathbf{r}}{\rho^2} = \frac{1}{\rho^2} S,$$

where $S \in C^\infty$. Bounds for the derivatives are

$$|\partial_{\mathbf{y}}^\beta \log \rho| \leq \frac{C}{\rho^{|\beta|+1}}, \quad \left| \partial_{\mathbf{y}}^\beta \frac{\mathbf{r} \otimes \mathbf{r}}{\rho^2} \right| \leq \frac{C}{\rho^{|\beta|+2}},$$

where β is a multi-index of order $|\beta| \leq M$. If $\rho > \sqrt{h}$, then the M^{th} -order derivatives are bounded by $Ch^{-M/2-1}$, and the error introduced by the N -point trapezoid rule satisfies

$$\epsilon_{\text{trap}} \leq h^M \cdot Ch^{-M/2-1} = Ch^{M/2-1}.$$

We would like to achieve the same accuracy when $\rho \in (h, \sqrt{h}]$. If $\rho \in (h, \sqrt{h}]$, the M^{th} -order derivatives are bounded by Ch^{-M-2} , and the error introduced by the $N^{3/2}$ -point trapezoid rule satisfies

$$\epsilon_{\text{trap}} \leq h^{3M/2} \cdot Ch^{-M-2} = Ch^{M/2-2}.$$

Therefore, in what we have defined as the far zone, the error in the trapezoid rule is $\mathcal{O}(h^{M/2-2})$.

To bound the error in the far zone of the double-layer potential, we note that

$$\left| \partial_{\mathbf{y}}^\beta \frac{\mathbf{r} \cdot \mathbf{n}}{\rho^2} \frac{\mathbf{r} \otimes \mathbf{r}}{\rho^2} \right| \leq \frac{C}{\rho^{|\beta|+4}}.$$

We repeat the same calculation done for the single-layer potential and the result is that the error in the far zone of the $N^{3/2}$ -point trapezoid rule applied to the double-layer potential is $\mathcal{O}(h^{M/2-4})$.

For the near zone, we find the solution using $m+1$ Lagrange interpolation points. All the interpolation points except for the first lie in the far zone and the above error bounds hold at these points. The Lagrange interpolation point on γ is computed using N_{int} interpolation points, so its error is $\mathcal{O}(h^{N_{\text{int}}-1})$. Combining the three approximations, the error of our near-singular integration scheme for the single-layer potential is

$$\mathcal{O}\left(h^{\min(N_{\text{int}}-1, m, \frac{M}{2}-2)}\right),$$

and for the double-layer potential is

$$\mathcal{O}\left(h^{\min(N_{\text{int}}-1, m, \frac{M}{2}-4)}\right).$$

B. Jumps in pressure and stress

We compute the jumps in the pressure and the stress of the single-layer potential. Consider a vesicle ω with boundary γ , normal vector \mathbf{n} , tangent vector $\boldsymbol{\tau}$, and traction jump \mathbf{f} . Then, the pressure due to the single-layer potential is

$$\begin{aligned} p(\mathbf{x}) &= \frac{1}{2\pi} \int_{\gamma} \frac{\mathbf{r} \cdot \mathbf{f}}{\rho^2} ds_{\mathbf{y}} \\ &= \frac{1}{2\pi} \int_{\gamma} \frac{(\mathbf{r} \cdot \mathbf{n})}{\rho^2} (\mathbf{f} \cdot \mathbf{n}) ds_{\mathbf{y}} + \frac{1}{2\pi} \int_{\gamma} \frac{(\mathbf{r} \cdot \boldsymbol{\tau})}{\rho^2} (\mathbf{f} \cdot \boldsymbol{\tau}) ds_{\mathbf{y}}. \end{aligned}$$

Both integrals are layer potentials of Laplace's equation. The first is the double-layer potential with density $\mathbf{f} \cdot \mathbf{n}$ and the second is the adjoint of the tangential derivative of the single-layer potential with density $\mathbf{f} \cdot \boldsymbol{\tau}$.

Standard potential theory [15] shows that the first integral has a jump of size 1/2 while the second integral has no jump. Therefore,

$$\begin{aligned}\lim_{\substack{\mathbf{x} \rightarrow \mathbf{x}_0 \\ \mathbf{x} \in \omega}} p(\mathbf{x}) &= +\frac{1}{2} \mathbf{f}_0 \cdot \mathbf{n}_0 + p(\mathbf{x}_0), \\ \lim_{\substack{\mathbf{x} \rightarrow \mathbf{x}_0 \\ \mathbf{x} \notin \omega}} p(\mathbf{x}) &= -\frac{1}{2} \mathbf{f}_0 \cdot \mathbf{n}_0 + p(\mathbf{x}_0),\end{aligned}$$

where $\mathbf{f}_0 = \mathbf{f}(\mathbf{x}_0)$ and $\mathbf{n}_0 = \mathbf{n}(\mathbf{x}_0)$.

To find the jump in the stress tensor, we decompose it into its tangential and normal components

$$\begin{aligned}T[\boldsymbol{\sigma}](\mathbf{x}) &= \frac{1}{\pi} \int_{\gamma} \frac{\mathbf{r} \otimes \mathbf{r} \mathbf{r} \cdot \boldsymbol{\sigma}}{\rho^2} \mathbf{f} ds \\ &= \frac{1}{\pi} \int_{\gamma} \frac{\mathbf{r} \otimes \mathbf{r} \mathbf{r} \cdot \mathbf{n}}{\rho^2} (\boldsymbol{\sigma} \cdot \mathbf{n}) \mathbf{f} ds + \frac{1}{\pi} \int_{\gamma} \frac{\mathbf{r} \otimes \mathbf{r} \mathbf{r} \cdot \boldsymbol{\tau}}{\rho^2} (\boldsymbol{\sigma} \cdot \boldsymbol{\tau}) \mathbf{f} ds \\ &=: T_{\mathbf{n}}[(\boldsymbol{\sigma} \cdot \mathbf{n})\mathbf{f}](\mathbf{x}) + T_{\boldsymbol{\tau}}[(\boldsymbol{\sigma} \cdot \boldsymbol{\tau})\mathbf{f}](\mathbf{x}).\end{aligned}$$

We use the usual method of placing a target point $\mathbf{x}_0 \in \gamma$, deforming the boundary by adding a circle of radius ϵ at \mathbf{x}_0 , computing the integral around the circle, and letting ϵ tend to zero. However, we first rotate the tensors $T_{\mathbf{n}}$ and $T_{\boldsymbol{\tau}}$ by the matrix R so that the normal and tangential vectors at \mathbf{x}_0 are $(1, 0)$ and $(0, 1)$ respectively. Using the Residue Theorem to compute the contribution from the half circle, the jumps are

$$\lim_{\substack{\mathbf{x} \rightarrow \mathbf{x}_0 \\ \mathbf{x} \notin \omega}} RT_{\mathbf{n}}[\mathbf{f}](\mathbf{x})R^T = \frac{1}{2} \begin{bmatrix} 1 & 0 \\ 0 & 1 \end{bmatrix} \mathbf{f}(\mathbf{x}_0) + RT_{\mathbf{n}}[\mathbf{f}](\mathbf{x}_0)R^T, \quad (9)$$

$$\lim_{\substack{\mathbf{x} \rightarrow \mathbf{x}_0 \\ \mathbf{x} \notin \omega}} RT_{\boldsymbol{\tau}}[\mathbf{f}](\mathbf{x})R^T = \frac{1}{2} \begin{bmatrix} 0 & 1 \\ 1 & 0 \end{bmatrix} \mathbf{f}(\mathbf{x}_0) + RT_{\boldsymbol{\tau}}[\mathbf{f}](\mathbf{x}_0)R^T. \quad (10)$$

If the limits are taken with $\mathbf{x} \in \omega$, the sign in the jump changes to $-1/2$. By left multiplying (9) and (10) by R^T and right multiplying by R , the jump in $T[\boldsymbol{\sigma}](\mathbf{x})$ from the interior of the vesicle is (7) and from the exterior of the vesicle is (8).

C. Variable curvature formulation

The traction jump \mathbf{f} minimizes the energy functional $\int_{\gamma} \frac{\kappa_b}{2} \kappa^2 ds$ subject to the inextensibility constraint. An alternative traction jump is derived by minimizing

$$\int_{\gamma} \frac{\kappa_b}{2} (\kappa - \tilde{\kappa})^2 ds, \quad \text{subject to } \|\mathbf{x}_s\| = 1, \quad (11)$$

where $\tilde{\kappa}$ is the curvature of a prescribed intrinsic vesicle shape whose perimeter we are assuming is one. By taking the first variation of (11), the force due to bending is

$$\mathbf{f}_b = \left(\kappa_{ss} + \frac{\kappa^3}{2} - \tilde{\kappa}_{ss} - \frac{\kappa \tilde{\kappa}^2}{2} \right) \mathbf{n} + (\kappa - \tilde{\kappa}) \tilde{\kappa}_s \mathbf{t}.$$

It is shown in [40] that terms of the form $(h(s)\mathbf{x}_s)_s$ do no work for inextensible vesicles and hence such forces can be added to modify \mathbf{f}_b . A convenient choice is $h(s) = 3/2 \kappa^2 - 1/2 \tilde{\kappa}^2$ which results in the simpler traction jump

$$\mathbf{f} = \mathbf{f}_b + \mathbf{f}_{\sigma} = \kappa_b (-\mathbf{x}_{ssss} - \tilde{\kappa}_{ss} \mathbf{n} - \kappa \tilde{\kappa}_s \mathbf{t}) + (\boldsymbol{\sigma} \mathbf{x}_s)_s.$$

We present simulations for several choices of $\tilde{\kappa}$ in Figure 10. The flow is only driven by the vesicle configuration since there is no background flow. For $\tilde{\kappa}$, we take the curvature of an ellipse with an aspect ratio of 1 (top plots), 2 (middle plots), and 4 (bottom plots). We see that the curvature of the vesicle tries to fit to the curvature of the intrinsic shape while maintaining its area and arclength.

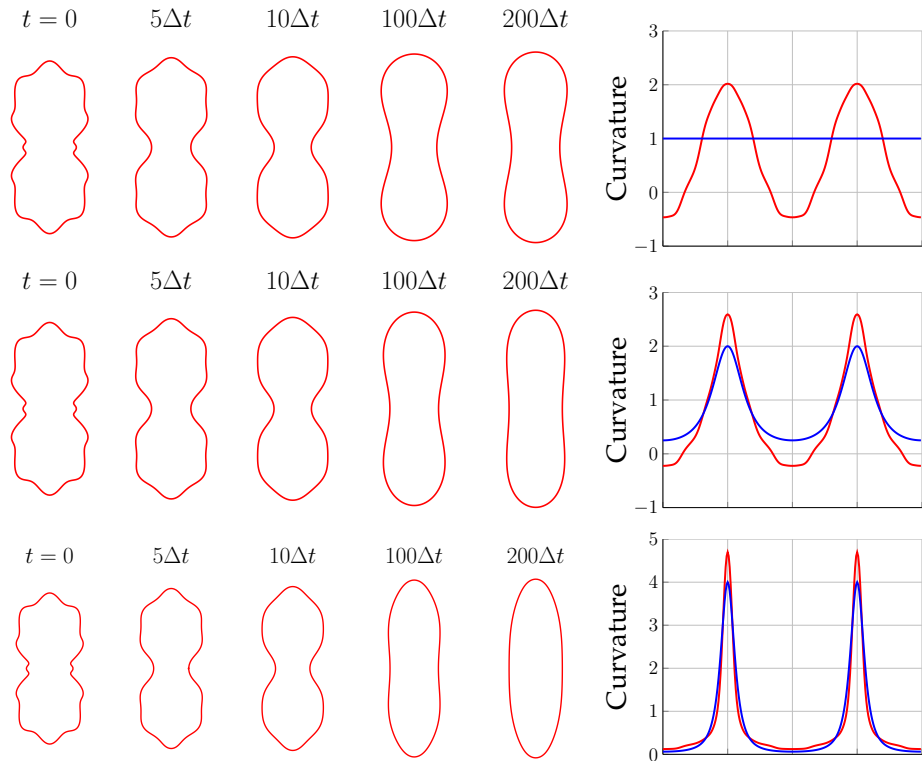


Figure 10: Here we show the relaxation dynamics of a single vesicle with three different prescribed intrinsic curvatures $\bar{\kappa}$. There is no imposed background flow. The vesicle is discretized with $N = 256$ points and $\Delta t = 0.02$. After 200 time steps, the vesicle is within 0.01% of its steady state configuration. The final curvature (red) and curvature of the intrinsic shape (blue) are in the right plots.

References

- [1] B. K. Alpert. Hybrid Gauss-trapezoidal quadrature rules. *SIAM Journal on Scientific Computing*, 20: 1551–1584, 1999.
- [2] U. M. Ascher, S. J. Ruuth, and B. T. R. Wetton. Implicit-explicit methods for time dependent partial differential equations. *SIAM Journal on Numerical Analysis*, 32:797–823, 1995.
- [3] P. Dimitrakopoulos. Interfacial dynamics in Stokes flow via a three-dimensional fully-implicit interfacial spectral boundary element algorithm. *Journal of Computational Physics*, 225:408–426, 2007.
- [4] P. Dimitrakopoulos and J. J. L. Higdon. Displacement of fluid droplets from solid surfaces in low-Reynolds-number shear flows. *Journal of Fluid Mechanics*, 336:351–378, 1997.
- [5] A. Dutt, L. Greengard, and V. Rokhlin. Spectral Deferred Correction Methods for Ordinary Differential Equations. *BIT Numerical Mathematics*, 40:241–266, 2000.
- [6] J. B. Freund and H. Zhao. *A high-resolution fast boundary-integral method for multiple blood cells*, chapter 3, pages 71–111. CRC Press, 2010.
- [7] Jonathan B. Freund and M. M. Orescanin. Cellular flow in a small blood vessel. *Journal of Fluid Mechanics*, 671:466–490, 2011.
- [8] G. Ghigliotti, A. Rahimian, G. Biros, and C. Misbah. Vesicle migration and spatial organization driven by flow line curvature. *Physical Review Letters*, 106:028101, 2011.
- [9] Johan Helsing and Rikard Ojala. Corner singularities for elliptic problems: Integral equations, graded meshes, quadrature, and compressed inverse preconditioning. *Journal of Computational Physics*, 227: 8820–8840, 2008.
- [10] Jingfang Huang, Jun Jia, and Michael Minion. Arbitrary order Krylov deferred correction methods for differential algebraic equations. *Journal of Computational Physics*, 221(2):739–760, 2007.
- [11] Pablo Jiménez, Federico Thomas, and Carme Torras. 3D collision detection: A survey. *Computers & Graphics*, 25(2):269–285, 2001.
- [12] V. Kantsler and V. Steinberg. Transition to tumbling and two regimes of tumbling motion of a vesicle in shear flow. *Physical Review Letters*, 96(3), 2006.
- [13] B. Kaoui, N. Tahiri, T. Biben, H. Ez-Zahraouy, A. Benyoussef, G. Biros, and C. Misbah. What Dictates Red Blood Cell Shapes and Dynamics in the Microvasculature? *Physical Review E*, pages 1–11, 2011.
- [14] Badr Kaoui, George Biros, and Chaouqi Misbah. Why Do Red Blood Cells Have Asymmetric Shapes Even in a Symmetric Flow? *Physical Review Letters*, 103(18):188101, 2009.
- [15] O. D. Kellogg. *Foundations of Potential Theory*. Dover, 1953.
- [16] Andreas Klöckner, Alexander Barnett, Leslie Greengard, and Michael O’Neil. Quadrature by Expansion: A New Method for the Evaluation of Layer Potentials. <http://arxiv.org/abs/1207.4461>, 2012.
- [17] M. Kraus, W. Wintz, U. Seifert, and R. Lipowsky. Fluid Vesicles in Shear Flow. *Physical Review Letter*, 77(17):3685–3688, 1996.
- [18] R. Kress. *Linear Integral Equations*. Applied Mathematical Sciences. Springer, 2nd edition, 1999.
- [19] M. C. A. Kropinski. Integral Equation Methods for Particle Simulations in Creeping Flows. *Computers and Mathematics with Applications*, 38:67–87, 1999.

- [20] Amit Kumar and Michael D. Graham. Segregation by membrane rigidity in flowing binary suspensions of elastic capsules. *Physical Review E*, 84, 2011.
- [21] Amit Kumar, Rafael G. Henriuez Rivera, and Michael D. Graham. Flow-induced segregation in confined multicomponent suspensions: effects of particle size and rigidity. *Journal of Fluid Mechanics*, 738: 423–462, 2014.
- [22] X. Li and C. Pozrikidis. Film flow of a suspension of liquid drops. *Physics of Fluids*, 14(1), 2002.
- [23] Michael L. Minion. Semi-Implicit Spectral Deferred Correction Methods for Ordinary Differential Equations. *Communications in Mathematical Sciences*, 1(3):471–500, 2003.
- [24] C. Misbah. Vacillating breathing and tumbling of vesicles under shear flow. *Physical Review Letters*, 96(2), 2006.
- [25] H. Noguchi and D. G. Gompfer. Shape transitions of fluid vesicles and red blood cells in capillary flows. *Proceedings Of The National Academy Of Sciences Of The United States Of America*, 102:14159–14164, 2005.
- [26] C. Pozrikidis. The Axisymmetric Deformation Of A Red Blood Cell In Uniaxial Straining Stokes Flow. *Journal of Fluid Mechanics*, 216:231–254, 1990.
- [27] C. Pozrikidis. *Boundary Integral and Singularity Methods for Linearized Viscous Flow*. Cambridge University Press, New York, NY, USA, 1992.
- [28] C. Pozrikidis. A Spectral-Element Method for Particulate Stokes Flow. *Journal of Computational Physics*, 156:360–381, 1999.
- [29] C. Pozrikidis. Interfacial dynamics for Stokes flow. *Journal of Computational Physics*, 169:250–301, 2001.
- [30] C. Pozrikidis. Effect of membrane bending stiffness on the deformation of capsules in simple shear flow. *Journal of Fluid Mechanics*, 440:269–291, 2001.
- [31] Patrik Pranay, Rafael G. Henriquez-Rivera, and Michael D. Graham. Depletion layer formation in suspensions of elastic capsules in Newtonian and viscoelastic fluids. *Physics of Fluids*, 24, 2012.
- [32] Bryan Quaife and George Biros. On preconditioners for the Laplace double-layer in 2D. <http://arxiv.org/abs/1308.1937>, 2013.
- [33] Abtin Rahimian, Shravan Kumar Veerapaneni, and George Biros. Dynamic simulation of locally inextensible vesicles suspended in an arbitrary two-dimensional domain, a boundary integral method. *Journal of Computational Physics*, 229:6466–6484, 2010.
- [34] Stephane Redon, Young J. Kim, Ming C. Lin, and Dinesh Manocha. Fast continuous collision detection for articulated models. In *Proceedings of the ninth ACM Symposium on Solid Modeling and Applications*, pages 145–156. Eurographics Association, 2004.
- [35] Y. Saad. *Iterative Methods for Sparse Linear Systems*. Society for Industrial and Applied Mathematics, Philadelphia, PA, USA, second edition, 2003.
- [36] E. Sackmann. Supported membranes: Scientific and practical applications. *Science*, 271:43–48, 1996.
- [37] David Salac and Michael J. Miksis. Reynolds number effect on lipid vesicles. *Journal of Fluid Mechanics*, 711:122–146, 2012.
- [38] U. Seifert. Configurations of fluid membranes and vesicles. *Advances in Physics*, 46:13–137, 1997.
- [39] Avram Sidi and Moshe Israeli. Quadrature Methods for Periodic Singular and Weakly Singular Fredholm Integral Equations. *Journal of Scientific Computing*, 3(2):201–231, 1988.

- [40] S. K. Veerapaneni, D. Gueyffier, D. Zorin, and G. Biros. A boundary integral method for simulating the dynamics of inextensible vesicles suspended in a viscous fluid in 2D. *Journal of Computational Physics*, 228(7):2334–2353, 2009.
- [41] Shravan K. Veerapaneni, Abtin Rahimian, George Biros, and Denis Zorin. A fast algorithm for simulating vesicle flows in three dimensions. *Journal of Computational Physics*, 230(14):5610–5634, 2011.
- [42] Lexing Ying, George Biros, and Denis Zorin. A kernel-independent adaptive fast multipole method in two and three dimensions. *Journal of Computational Physics*, 196(2):591–626, 2004.
- [43] Lexing Ying, George Biros, and Denis Zorin. A high-order 3D boundary integral equation solver for elliptic PDEs in smooth domains. *Journal of Computational Physics*, 219(1):247–275, 2006.
- [44] H. Zhao and E. S. G. Shaqfeh. The dynamics of a vesicle in shear flow. Technical report, Stanford University, 2009.
- [45] Hong Zhao and Eric S. G. Shaqfeh. The dynamics of a vesicle in simple shear flow. *Journal of Fluid Mechanics*, 674:578–604, 2011.
- [46] Hong Zhao and Eric S. G. Shaqfeh. Shear-induced platelet margination in a microchannel. *Physical Review E*, 83, 2011.
- [47] Hong Zhao and Eric S. G. Shaqfeh. The shape stability of a lipid vesicle in a uniaxial extensional flow. *Journal of Fluid Mechanics*, 719:345–361, 2013.
- [48] Hong Zhao and Eric S. G. Shaqfeh. The dynamics of a non-dilute vesicle suspension in simple shear flow. *Journal of Fluid Mechanics*, 725:709–731, 2013.
- [49] Hong Zhao, Amir H.G. Isfahani, Luke N. Olson, and Jonathan B. Freund. A spectral boundary integral method for flowing blood cells. *Journal of Computational Physics*, 229:3726–3744, 2010.
- [50] Hong Zhao, Eric S. G. Shaqfeh, and Vivek Narsimhan. Shear-induced particle migration and margination in a cellular suspension. *Physics of Fluids*, 24, 2012.